

## LINE DERIVED INFRARED EXTINCTION TOWARD THE GALACTIC CENTER

T. K. FRITZ<sup>1</sup>, S. GILLESSEN<sup>1</sup>, K. DODDS-EDEN<sup>1</sup>, D. LUTZ<sup>1</sup>, R. GENZEL<sup>1,2</sup>, W. RAAB<sup>1</sup>, T. OTT<sup>1</sup>, O. PFUHL<sup>1</sup>, F. EISENHAEUER<sup>1</sup>,  
 AND F. YUSEF-ZADEH<sup>3</sup>

<sup>1</sup> Max-Planck-Institut für Extraterrestrische Physik, Postfach 1312, D-85741 Garching, Germany

<sup>2</sup> Department of Physics, University of California, Berkeley, 366 Le Conte Hall, Berkeley, CA 94720-7300, USA

<sup>3</sup> Department of Physics and Astronomy, Northwestern University, Evanston, IL 60208, USA

Received 2011 April 18; accepted 2011 May 17; published 2011 August 8

### ABSTRACT

We derive the extinction curve toward the Galactic center (GC) from 1 to 19  $\mu\text{m}$ . We use hydrogen emission lines of the minispiral observed by ISO-SWS and SINFONI. The extinction-free flux reference is the 2 cm continuum emission observed by the Very Large Array. Toward the inner  $14'' \times 20''$ , we find an extinction of  $A_{2.166\mu\text{m}} = 2.62 \pm 0.11$ , with a power-law slope of  $\alpha = -2.11 \pm 0.06$  shortward of 2.8  $\mu\text{m}$ , consistent with the average near-infrared slope from the recent literature. At longer wavelengths, however, we find that the extinction is *grayer* than shortward of 2.8  $\mu\text{m}$ . We find that it is not possible to fit the observed extinction curve with a dust model consisting of pure carbonaceous and silicate grains only, and the addition of composite particles, including ices, is needed to explain the observations. Combining a distance-dependent extinction with our distance-independent extinction, we derive the distance to the GC to be  $R_0 = 7.94 \pm 0.65$  kpc. Toward Sgr A\* ( $r < 0''.5$ ), we obtain  $A_H = 4.21 \pm 0.10$ ,  $A_{K_s} = 2.42 \pm 0.10$ , and  $A_{L'} = 1.09 \pm 0.13$ .

**Key words:** dust, extinction – Galaxy: center – Galaxy: fundamental parameters

**Online-only material:** color figures, machine-readable table

### 1. INTRODUCTION

Knowledge of the extinction in the infrared (Schultz & Wiemer 1975; Cardelli et al. 1989; Mathis 1990) is important for obtaining the intrinsic luminosities of highly extinguished objects. In addition, the extinction curve provides important constraints on the properties of interstellar dust (see, e.g., Compiègne et al. 2011). Using the extinction curve together with the dust emission, it is possible to derive the composition and sizes of interstellar dust grains. In this way it has been found that interstellar dust is mainly composed of silicate and carbonaceous dust grains (Draine 2003). However, it is still uncertain if composite particles are also required (Mathis 1996; Li & Greenberg 1997; Weingartner & Draine 2001; Zubko et al. 2004), including, for example, ices and voids in addition to the basic dust grains.

The Galactic center (GC), invisible in the optical, is one well-known example of a highly extinguished region (Becklin & Neugebauer 1968). Because of this, it should be relatively easy to measure the infrared extinction, without the large relative errors implicated in using regions of small absolute extinction. Rieke & Lebofsky (1985), for example, used infrared photometry of a few red supergiants present in the GC together with a visible to near-infrared extinction law obtained outside of the GC, in order to derive a universal infrared extinction law (Figure 1). This measurement was later slightly improved by adding NICMOS near-infrared measurements by Rieke (1999).

Another method of measuring the IR extinction is to use a stellar population of known infrared luminosity (Nishiyama et al. 2006b), such as the red clump for which the absolute luminosity is measured locally (Groenewegen 2008). For this method, however, it is also necessary to know a precise distance to the object, which makes the method difficult for most objects. In the case of the GC however the distance is well known (Reid 1993; Genzel et al. 2010). Using this method, Schödel et al. (2010) obtained  $A_H = 4.35 \pm 0.18$ ,  $A_{K_s} = 2.46 \pm 0.12$ , and  $A_{L'} = 1.23 \pm 0.20$  toward Sgr A\*.

As an alternative to methods involving stars, one can also use nebular hydrogen lines to measure extinction. As a case in point, Lutz et al. (1996) and Lutz (1999) used spectra from the Short Wave Spectrometer of the *Infrared Space Observatory* (ISO-SWS) of the minispiral (a bright H II region in the GC; Lo & Claussen 1983) to derive extinction from 2.6 to 19  $\mu\text{m}$ . Typically, this method is more precise, since the intrinsic uncertainty of the relative line strengths in this case (Hummer & Storey 1987) is smaller than the spectral uncertainty of stellar emission. An additional advantage is that the lines are much narrower than the bandpasses of the broadband filters, so that the effective wavelength is known a priori, while for broadband filters it is extinction dependent. Furthermore, there are many more lines in the IR than the number of broadband filters in frequent use, such that it is easier to obtain a well-sampled extinction curve, that includes also extinction features.

Although it is only possible, using infrared lines alone, to obtain *relative* extinction measurements within the infrared, stellar methods often have the same problem. Absolute extinction calibration is made possible by comparing with longer wavelengths where the extinction is negligible. The absolute extinction toward the GC for the Paschen- $\alpha$  line at 1.87  $\mu\text{m}$  was obtained in this way in Scoville et al. (2003) using 6 cm continuum data.

The extinction toward Sgr A\* from the various measurements mentioned above is shown in Figure 1. However, there is apparently some discrepancy between the different studies. The uncertainty in extinction creates, in turn, uncertainty in determining the intrinsic luminosities of young massive stars in the GC (Martins et al. 2007; Fritz et al. 2010), as well as the intrinsic luminosity of Sgr A\* (Genzel et al. 2003). In addition, there is no study that covers the full wavelength range, and only a few studies of this kind are available outside of the GC.

In this paper, we use the emission of the minispiral from 1.28 to 19  $\mu\text{m}$  to derive relative extinction values from line emission, which are compared to 2 cm radio continuum data to compute the absolute extinction. In Section 2, we present our data and discuss the extraction of line maps and flux calibration in

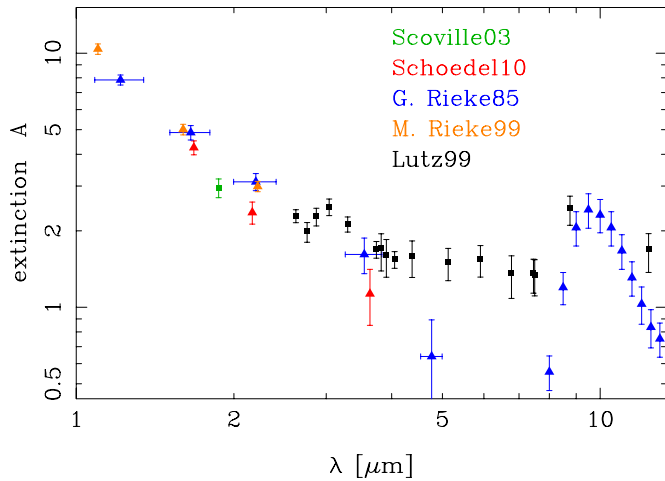


**Figure 1.** Extinction toward Sgr A\* from the literature: triangles represent values derived from stars, and boxes represent values derived from gas lines. Most values were obtained using slightly different regions around Sgr A\*. For the comparison, we convert the values to the direct sight line toward Sgr A\* (i.e., the central 0'.5, see Section 5.3) using the extinction map of Schödel et al. (2010). In the case of Rieke & Lebofsky (1985), we use the extinction law of Rieke & Lebofsky (1985) and the absolute extinction of Rieke et al. (1989).

(A color version of this figure is available in the online journal.)

Section 3. In Section 4, we derive the extinction. We discuss the results in Section 5. We compare the results with other works for the GC and for other parts of the Galaxy and with theoretical dust models. We also use the data for estimating the distance to the GC,  $R_0$ . We summarize in Section 6.

## 2. DATA SET

In this section, we describe the observations used to derive the extinction curve toward the GC. We used a Very Large Array (VLA) radio (2 cm continuum) map, ISO-SWS spectra (2.4–45  $\mu\text{m}$ ) and SINFONI imaging spectroscopy (1.2–2.4  $\mu\text{m}$ ), of which the latter is used to construct line maps at Brackett- $\gamma$  (2.166  $\mu\text{m}$ ), Brackett- $\zeta$  (1.736  $\mu\text{m}$ ), and Paschen- $\beta$  (1.283  $\mu\text{m}$ ). The fields of view for the different data sets are compared in Figure 2.

### 2.1. Radio

Figure 2 presents the radio and near-infrared data used combined with the field of views of all measurements. The radio data consist of combined 2 cm continuum observations in the A, B, C, and D configurations of the VLA. The phase center of the multi-configuration data set at 2 cm is on Sgr A\*. Standard calibration was done on each data set before each data set was combined in the  $uv$  plane. Details of phase and amplitude calibration of each data set taken in different configurations of the VLA can be found in Yusef-Zadeh & Wardle (1993) and Yusef-Zadeh et al. (1998). The combination of these configurations makes high resolution possible, while at the same time ensuring good coverage of extended structure. Due to the use of the smallest, D, configuration, we are able to detect structures of up to 50'' in size. The resolution of the final image is  $0'.42 \times 0'.3$  with the longer axis of the Gaussian oriented approximately north (P.A.  $\approx 4^\circ$ ). The image extends at least 48'' from Sgr A\* in all directions. We use a radio continuum map because, for the data available to us, the signal-to-noise ratio (S/N) and the resolution are better than for line maps.

We chose to use a map at 2 cm because non-thermal emission, redder than the thermal emission of the minispiral, is less

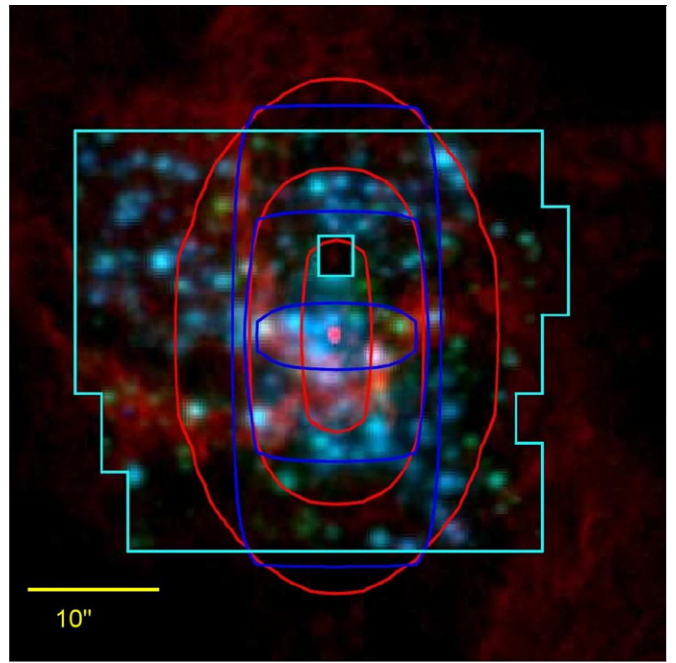


**Figure 2.** Field of view for different measurements. In red, the radio 2 cm continuum image; in blue and green, respectively, are the  $H$  and  $K_s$  broadband images constructed from SINFONI HK data. The radio image is larger than displayed here, but the outer areas are not used in this publication. Light green lines mark the borders of the SINFONI field which has a hole around IRS7. Blue lines indicate the contours of the ISO PSF around 2.6  $\mu\text{m}$ , representing 90%, 50%, and 10% of the central intensity. The red lines indicate the same for the ISO PSF around 19  $\mu\text{m}$ .

(A color version of this figure is available in the online journal.)

dominant at shorter wavelengths (Scoville et al. 2003, on the other hand, used a 6 cm map). Naturally, some non-thermal contamination is expected at 2 cm as well. We control for this by testing whether there is a correlation between minispiral emission and extinction strength (see Section 4.2). Sgr A\* is a clearly visible non-thermal source in the radio map, see Figure 2. However, due to our high resolution it is well isolated from the minispiral. We are thus able to fit the source by a Gaussian and subtract it, smoothing the area around it. As a result, Sgr A\* is not visible in our final radio map (Figure 3).

Two particularly problematic regions are IRS2 and IRS13, for which Roberts et al. (1996) and Shukla et al. (2004) derived significantly higher than average electron temperatures. In our analysis we simply ignore these regions, masking out IRS13 and IRS2.

Difficulties can also arise, for interferometric observations, from the fact that only a finite range of spatial frequencies can be sampled. This has the consequence that structure larger than the fringe spacing of the shortest baseline is not measured, which can result in an underestimate of the flux, if the observed object is much larger than the largest angular scale sampled. For us, however, this is not a problem, since with our map, due to the use of D configuration as mentioned above, we are able to detect structures of sizes up to 50'', while nearly all of the flux of the minispiral is concentrated within 50'' diameter (Figure 1 of Scoville et al. 2003).

### 2.2. ISO

We use the ISO-SWS data of Lutz (1999). These data are reduced with the SWS interactive analysis system (Wieprecht

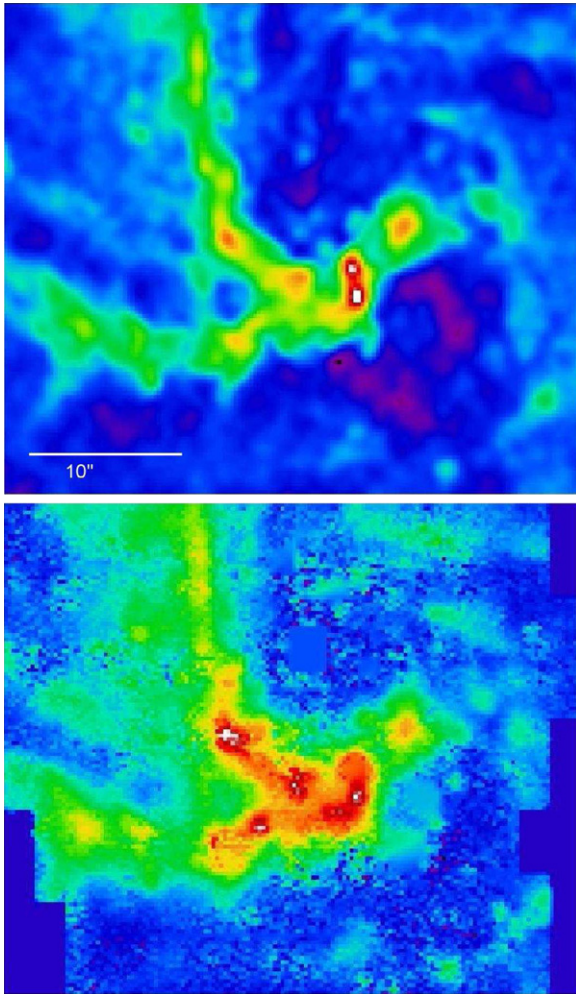


**Figure 3.** Top: 2 cm continuum radio image from VLA. We subtracted Sgr A\* by fitting a Gaussian to it. The resolution is smoothed to  $0''.85$ . Bottom: Brackett- $\gamma$  map derived from SINFONI. Areas with stellar lines are replaced by the neighboring gas emission. Some areas at the border were not mapped and are given zero flux. We fill the area around IRS7 that was not covered by the observations with the median flux of the surrounding. Both maps show the same area, with  $250 \text{ mas pixel}^{-1}$ , the same resolution, and the same color scaling. (A color version of this figure is available in the online journal.)

et al. 1998). The data consist of a single aperture spectrum extending from  $2.4$  to  $45 \mu\text{m}$ , shown in Figure 4.

The field of view of SWS (de Graauw et al. 1996a) is approximately rectangular; it can be seen in Figure 2. We consider the deviations from rectangularity (Beintema et al. 2003) in Section 3.2. In our observations, the longer axis of the field of view is oriented north–south (P.A.  $\approx 0^\circ$ ). The field of view is approximately  $14'' \times 20''$  shortward of  $12 \mu\text{m}$ , and  $14'' \times 27''$  between  $12$  and  $28 \mu\text{m}$ . The observations are centered on Sgr A\*.

### 2.3. SINFONI

For shorter wavelengths ( $1.2$ – $2.4 \mu\text{m}$ ), we use spectra obtained with the integral field spectrometer SINFONI (Eisenhauer et al. 2003b; Bonnet et al. 2003) at UT4 of the Very Large Telescope.<sup>4</sup> We use the following data:  $H+K$  band (spectral resolution 1500), seeing-limited cubes

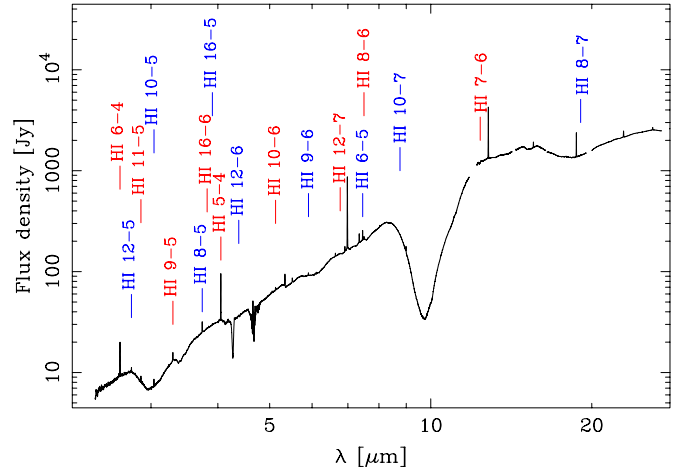


**Figure 4.** ISO-SWS spectrum of the GC. The hydrogen lines used for the extinction measurements are marked by colored vertical lines. (A color version of this figure is available in the online journal.)

(FWHM =  $0''.85$ ) covering an area of about  $37'' \times 30''$  around Sgr A\* from 2003 April 9 with a spatial sampling of  $250 \text{ mas pixel}^{-1} \times 250 \text{ mas pixel}^{-1}$ , and  $J$  band (spectral resolution 2000), seeing-limited cubes (FWHM =  $0''.6$ – $1''$ ) of most areas of the minispiral obtained 2010 May 21 and July 6, with a spatial sampling of  $125 \text{ mas pixel}^{-1} \times 250 \text{ mas pixel}^{-1}$ . We apply the standard data reduction SPRED (Abuter et al. 2006; Schreiber et al. 2004) for SINFONI data, including detector calibrations (such as bad pixel correction, flat-fielding, and distortion correction) and cube reconstruction. The wavelength scale is calibrated with emission line lamps and fine tuned with atmospheric OH lines. The HK data are atmosphere corrected and kept in ADU count units. No conversion in energy is applied. We flux calibrate the  $J$ -band data with standards which were observed directly after the science observations, as is described in more detail in the next section. The Brackett- $\gamma$  map, one of three line maps derived from the SINFONI observations (described in the next section), can be seen in Figure 3.

## 3. CONSTRUCTION OF LINE MAPS AND FLUX CALIBRATION

### 3.1. Line Maps

In this section, we describe the construction of Brackett- $\gamma$ , Brackett- $\zeta$ , and Paschen- $\beta$  line maps from the SINFONI data, see Table 1. In order to do this, we integrate over the channels which contain the nebular emission and subtract the average of the adjacent spectral channels on both sides as background. The line maps contain the following types of artifacts, unrelated to the minispiral emission.

1. Bad pixels, in the sense of a large deviation of a few pixels from their neighbors. We identify them mostly manually.
2. Gaps between cubes, when not well aligned.
3. Emission and absorption line stars.

We interpolate these artifacts, treating them like bad pixels in the data reduction. We also replace the hole around IRS7 in our map with the median flux of the surrounding for obtaining line maps, see the Brackett- $\gamma$  map in Figure 3.

### 3.2. Flux Calibration

We flux calibrate the Brackett- $\gamma$  map with a NACO  $K_s$  image of the GC from 2006 April 29. On this day, a standard star was

<sup>4</sup> We use SINFONI data from ESO programs 70.A-0029(A), 183.B-100(P), and 183.B-100(R).



**Table 1**  
Combinations of Lines or Continuum used for Deriving Extinctions

Line A	Line B	Area Used (“Good” Area)
2 cm continuum	Brackett- $\gamma$	“ISO beam,” excluding: low Br- $\gamma$ flux, IRS16C, IRS16NE, IRS13, IRS2
Brackett- $\gamma$	Brackett- $\zeta$	“ISO beam,” excluding: low Br- $\gamma$ flux, Br- $\gamma$ /Br- $\zeta$ outliers, IRS16C, IRS16NE, IRS13, IRS2
Brackett- $\gamma$	Paschen- $\beta$	“ISO beam” inside the $J$ -band data, excluding: low Br- $\gamma$ flux, IRS16C, IRS16NE, IRS13, IRS2
Brackett- $\gamma$	ISO lines	In each case the adequate ISO beam

observed with a zero-point uncertainty of 0.06 mag. In order to translate this calibration to the SINFONI data, we extract a mock  $Ks$  image ( $F_{\text{SINFONI } Ks}$ ) from the SINFONI cube. This is done by multiplying the atmosphere corrected SINFONI data slice by slice with factors which represent the product of atmospheric and NACO  $Ks$ -filter transmission<sup>5</sup> for every slice. The factors are scaled such that their integral is one. In this way we calibrate a single SINFONI slice at the isophotal wavelength of the  $Ks$  band.

We measure the full flux in the NACO image and in  $F_{\text{SINFONI } Ks}$  over the area covered by the SINFONI data. We estimate the uncertainty of the cross-calibration by dividing the two images into nine parts and measuring the count ratio in each part. We obtain an uncertainty of 0.03 mag from the standard deviation of the nine count ratios.

In total we use the following factor for calibration of the Brackett  $\gamma$  line map:

$$f = \frac{F_{\lambda Ks} \lambda_{\text{iso } Ks}}{R \lambda_{\text{Br } \gamma}} 10^{-0.4 \text{ ZP}} \quad (1)$$

$$= \frac{F_{\lambda Ks} \lambda_{\text{iso } Ks}}{R \lambda_{\text{Br } \gamma}} 10^{-0.4 \left( \text{ZP}_{\text{NACO}} + 2.5 \log \frac{F_{\text{SINFONI } Ks}}{F_{\text{NACO } Ks}} \right)}. \quad (2)$$

Here,  $F_{\lambda Ks}$  is the  $Ks$  calibration of Vega (Tokunaga & Vacca 2005),  $R$  is the number of slices per  $\mu\text{m}$ , and ZP is the zero point in magnitudes of the SINFONI data. We assume an error of 0.03 mag for  $F_{\lambda Ks}$ . Because we use ADU spectral data, the amount of energy per ADU depends on wavelength. Since the calibration is at the isophotal wavelength (Tokunaga & Vacca 2005), we multiply  $F_{\lambda Ks}$  by  $\lambda_{\text{iso } Ks}/\lambda_{\text{Br } \gamma}$ . Compared to using a standard star, our calibration has the advantage that we use the same NACO data as Schödel et al. (2010) for calibration. In this way, we reduce the uncertainty when comparing our results with theirs, see Section 5.2.

We calibrate Brackett- $\zeta$  in a similar way to Brackett- $\gamma$ , using the integrated flux of an  $H$ -band NACO image from 2006 April 29, which is compared to an  $H$ -band image constructed from the SINFONI cube. The errors of the calibration are 0.05 mag (NACO zero point), 0.04 mag (cross-calibration), and 0.03 mag uncertainty from the conversion to energy ( $F_{\lambda H}$ ).

We use data cubes flux calibrated with standard stars for Paschen- $\beta$  (see Figure 5), because a flux calibrated GC image in the  $J$  band was not readily available. By comparing the fluxes of different standard stars from the two nights in 2010 April and July in which the data were obtained, we validate that the calibration is stable, with only 0.034 mag rms scatter and 0.005 mag bias over the  $J$ -band spectrum. We test the calibration accuracy further by comparing adjacent areas in the data from April and July. In doing so, we do not find signs of significant discontinuities in the Brackett- $\gamma$  to Paschen- $\beta$  ratio at the border between the two areas. We estimate the systematic calibration error to be the same as for Brackett- $\gamma$ : 0.075 mag.

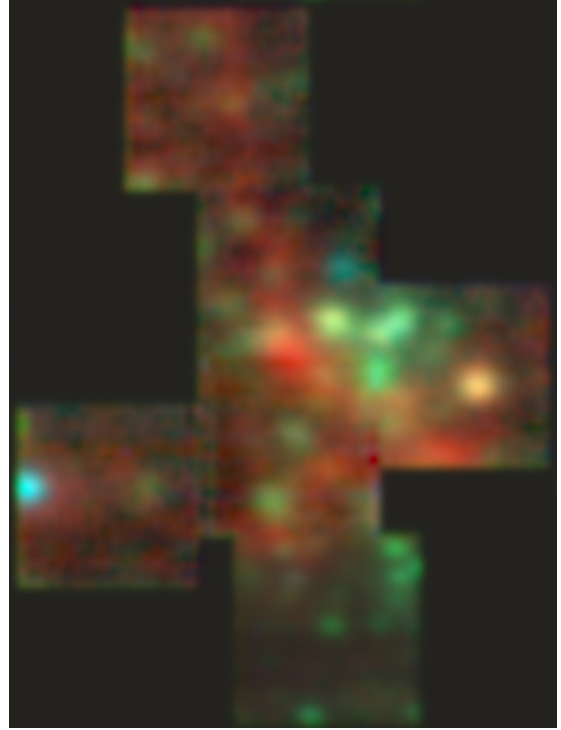


**Figure 5.** Color image from  $J$ -band SINFONI data: blue 1.18  $\mu\text{m}$  image, green 1.3  $\mu\text{m}$  image, and red Paschen- $\beta$  line map.

(A color version of this figure is available in the online journal.)

For the ISO data, we use the absolute calibration of Lutz et al. (1996). The calibration error dominates the total error for bright lines. It is 10% below 4.06  $\mu\text{m}$  and 20% above.

Since the emission of the minispiral is not homogeneous, it is necessary to compute the NIR and radio comparison fluxes from the same area as the ISO-SWS beam profile. Because of this we multiply the ISO-SWS beam profile (Beintema et al. 2003) in every ISO band with the Brackett- $\gamma$  line map and obtain the Brackett- $\gamma$  flux within the ISO-SWS beam profile. Since the Brackett- $\gamma$  map does not cover the full ISO beam, we also calculate the radio flux contained in the ISO-SWS beam profile in the same way. Over the Brackett- $\gamma$  field the difference in the beam correction is 3% between using radio and using Brackett- $\gamma$ . This difference could be caused by non-thermal emission. Therefore, we use the radio data only for calculating how much flux is missed due to the smaller field of the Brackett- $\gamma$  data. In total, we find that the flux is about 7% smaller below 12  $\mu\text{m}$  and about 6% higher above 12  $\mu\text{m}$  compared to a sharp  $14'' \times 20''$  field. The sudden change at 12  $\mu\text{m}$  is an artifact caused by the field size increase to  $14'' \times 27''$  at this wavelength.

#### 4. DERIVING EXTINCTION FROM HYDROGEN LINES

The ratios between different hydrogen recombination lines in H II regions depend only weakly on the local physics

<sup>5</sup> We use the NACO  $Ks$ -filter transmission from the NACO Web site: <http://www.eso.org/sci/facilities/paranal/instruments/naco/inst/filters.html>

(Hummer & Storey 1987). Hence, it is possible to derive the relative extinction ( $A$ ) between two lines  $a$  and  $b$  by comparing the observed flux ratio ( $F(a)_{\text{obs}}/F(b)_{\text{obs}}$ ) with the expected (extinction-free) flux ratio ( $F(a)_{\text{exp}}/F(b)_{\text{exp}}$ ):

$$A_{a-b} = -2.5 \times \log \left( \frac{F(a)_{\text{obs}}/F(b)_{\text{obs}}}{F(a)_{\text{exp}}/F(b)_{\text{exp}}} \right). \quad (3)$$

Using infrared data only, and without making further assumptions about the shape of the extinction curve, it is only possible to obtain the relative extinction. In order to obtain absolute extinction values, it is necessary to use a wavelength for  $b$  at which the extinction is known independently, or negligible. Then it is possible to calculate the expected flux at  $a$  from the observed flux at  $b$  using the known flux ratios for emission from a gaseous nebula (Baker & Menzel 1938). We use their Case B, for which the nebula is opaque to Lyman radiation but transparent to all other radiation (in Case A the nebula is also transparent to Lyman radiation):

$$F(a)_{\text{exp}} = c \times F(b)_{\text{obs}}, \quad (4)$$

$c$  follows from Case B calculation and depends on the radio frequency and infrared line used, as well as on the electron temperature, see also Section 4.1.

In our analysis, we use radio data for  $b$  and infrared lines in place of  $a$ . The formula for absolute extinction is thus

$$A_{\text{IR}} = -2.5 \times \log \left( \frac{F(\text{IR})_{\text{obs}}}{c \times F(\text{radio})_{\text{obs}}} \right). \quad (5)$$

We use Case B line ratios in Hummer & Storey (1987) for the  $F_{\text{obs}}$  ratios in formula (3). The unextincted ratios of hydrogen emission originating from different atomic levels depend on the radiation state (like Case B; Lutz 1999). As a first test of the validity of Case B, we use the hydrogen line in the ISO-SWS spectrum at  $7.50 \mu\text{m}$ , which is a blend of the lines 6–8 and 8–11. After accounting for the blending the  $7.50 \mu\text{m}$  extinction differs only by 0.05 mag from the extinction for the 6–5 line at  $7.46 \mu\text{m}$ , assuming Case B. This implies that Case B is indeed valid for the GC (Lutz 1999).

#### 4.1. Electron Temperature

The physical conditions of the plasma, in particular the electron temperature ( $T_e$ ), have an important influence on the extinction-free flux ratios of the IR line fluxes to the radio flux. For example, the dependence of Paschen  $\alpha$  to radio continuum (free–free) emission ( $S_{\text{ff}}$ ) is  $F_{\text{Pa}\alpha}/S_{\text{ff}} \propto T_e^{-0.52}$  (Scoville et al. 2003). Accordingly, it is necessary to know  $T_e$  for deriving the absolute extinction.

The electron temperature has been derived at H92 $\alpha$  (8.3 GHz) by Roberts & Goss (1993) and at H41 $\alpha$  (92 GHz) by Shukla et al. (2004). Both obtain  $T_e \approx 7000$  K in most parts of the minispiral. The consistency of both measurements shows that all conditions, thus also Case B (Roberts et al. 1991), for deriving  $T_e$  are fulfilled, even at the smaller and more problematic frequency of 8.3 GHz. In this work, we take the measurement by Roberts & Goss (1993) of  $T_e = 7000 \pm 500$  K, since it has the highest S/N, but we correct it to account for the He<sup>+</sup> fraction (see below).

According to Roberts & Goss (1993), there is no significant spatial variation in the electron temperature. Thus, we think that it is justified to simply assume a constant electron temperature.

Even if the electron temperature varies, the variation does not matter as long as the value used is equal to the flux-weighted average of  $T_e$  of the area over which we integrate.

The absolute value of  $T_e$  also depends on the He<sup>+</sup> fraction:  $Y^+ = \text{He}^+/\text{H}^+$ . Roberts & Goss (1993) derived a  $2\sigma$  limit for  $Y^+$  of 3%, and measured  $Y^+ = 5\% \pm 2\%$  in another area. Krabbe et al. (1991) derived  $Y^+ \approx 4\%$  from the He I line at  $2.06 \mu\text{m}$ . We obtain  $Y^+ = 2\% \pm 0.7\%$  using the same line. Considering all information, we assume  $Y^+ = 3\% \pm 1\%$  for the calculation of  $T_e$ .

The electron temperature depends, according to Roberts et al. (1996) and Roelfsema et al. (1992), in the following way on  $Y^+$ :

$$T_e = \left( T_{e,\text{raw}} \frac{1}{1 + Y^+} \right)^{0.87}, \quad (6)$$

where  $T_{e,\text{raw}}$  is the  $T_e$  obtained assuming  $Y^+ = 0$ . Since Roberts & Goss (1993) used  $Y^+ = 0$ , they calculated  $T_{e,\text{raw}}$ . We therefore calculate the real  $T_e$  from the  $T_{e,\text{raw}}$  of Roberts & Goss (1993) using our value of  $Y^+ = 3\%$ . We obtain  $T_e = 6800 \pm 500$  K and use this value hereafter. The error in the electron temperature results in an absolute extinction error of 0.043 mag. In principle, it is also necessary to know the electron density of the emitting plasma to calculate the absolute extinction from infrared lines and radio emission (Hummer & Storey 1987). We use an electron density of  $10^4 \text{ cm}^{-3}$  (Shukla et al. 2004), but the results are not very sensitive to the actual value used (Hummer & Storey 1987).

#### 4.2. Extinction Calculation

We first compute the Brackett- $\gamma$  extinction from direct comparison of the Brackett- $\gamma$  map with the radio data (Figure 3), following formula (5). We then calculate all other extinction values with respect to the Brackett- $\gamma$  data. This method has the advantage that we can select the fiducial area by comparing with the high S/N Brackett- $\gamma$  data (Table 1). This is done by calculating the extinction relative to Brackett- $\gamma$  extinction following formula (3). The Brackett- $\gamma$  extinction is then added to this value to obtain the absolute extinction.

To calculate the expected flux ratio, we convert formula (3) of Scoville et al. (2003) to Brackett- $\gamma$ , our continuum frequency of 15 GHz, and mJy, using the relative line strength in Hummer & Storey (1987):

$$\left( \frac{F_{\text{Br}\gamma}}{S_{\text{ff}}} \right)_{\text{exp}} = (1.327 \pm 0.052) 10^{-11} \text{ erg s}^{-1} \text{ cm}^{-2} \text{ mJy}^{-1}. \quad (7)$$

Inserting this expected ratio and the measured Brackett- $\gamma$  to radio ratio in formula (5), we obtain a Brackett- $\gamma$  extinction map.

In order to estimate the impact of non-thermal emission, we measure the resulting extinction in Brackett- $\gamma$  flux bins, see Figure 6. For most line fluxes, the extinction is approximately constant. However, for line fluxes smaller than  $3.7 \times 10^{-16} \text{ erg s}^{-1} \text{ cm}^{-2} \text{ pixel}^{-1}$  the extinction is anticorrelated with the Brackett- $\gamma$  flux. Most likely the anticorrelation is caused by non-thermal emission of Sgr A East which becomes more important in fainter regions of the minispiral. Because of this, we mask out areas with fluxes smaller than  $3.7 \times 10^{-16} \text{ erg s}^{-1} \text{ cm}^{-2} \text{ pixel}^{-1}$ . The choice of this flux cut is somewhat arbitrary. However, since we only use the integrated flux of the whole ISO beam, which is dominated by the brighter

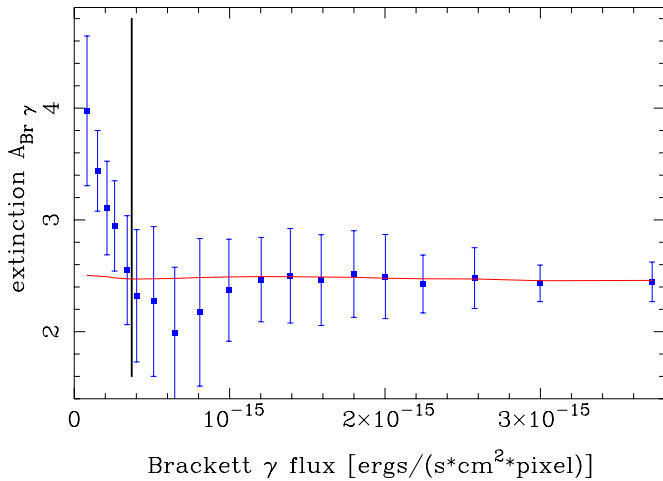


**Figure 6.** Extinction in the central  $14'' \times 20''$ , binned in Brackett- $\gamma$  flux. The squares and error bars mark the median extinction per flux bin. (The error is based on the median deviation, scaled to a Gaussian  $1\sigma$  error by multiplying it with 1.483.) While for small fluxes the extinction is anticorrelated with the flux, there is no such correlation at fluxes larger than the vertical line at  $3.7 \times 10^{-16} \text{ erg s}^{-1} \text{ cm}^{-2} \text{ pixel}^{-1}$ . The red line is the integrated extinction using all pixels with a flux larger than or equal to the flux in the given bin. There is nearly no variation.

(A color version of this figure is available in the online journal.)

fluxes, the uncertainty of the flux cut only introduces an extinction error of 0.03 mag. In addition, we mask out IRS2 and IRS13 (see Section 2.1), as well as IRS16NE and IRS16C because of remaining stellar emission line flux there.

The extinction in the areas defined by the above constraints is similar to the extinction map of Schödel et al. (2010). However, there is a scatter of about 0.4 mag in our map, when comparing pixel by pixel, due to the low S/N per pixel in Brackett- $\gamma$  and radio data. Because of this, our extinction map is not of direct use. Nevertheless, the small S/N per pixel does not affect our absolute measurement, because we use the flux from a total of 2854 pixels for deriving the Brackett- $\gamma$  extinction.

For a comparison with Schödel et al. (2010), we add up the Brackett- $\gamma$  and radio fluxes within 0.1 mag bins. We use the extinction map of Schödel et al. (2010) to bin according to extinction. We then calculate the extinction in every bin from the total fluxes therein by means of formula (7) (see Figure 7). The differences between the extinction values from Schödel et al. (2010) and this work have an rms scatter of 0.10 mag. This scatter is bigger than would be expected from the S/N of both maps, but systematic problems, such as residual anisoplanatism in Schödel et al. (2010), or  $T_e$  variations for our map, could cause increased scatter. We assume that half of the scatter is caused by our data and add therefore 0.07 mag as additional extinction error. This estimate is conservative, because many problems should average out over the full area.

Our aim is to measure the wavelength-dependent extinction curve in one line of sight. Spatially variable extinction can however cause deviation of the line-of-sight extinction curve, if different measurement areas are used at different wavelengths. In addition, for comparison with Schödel et al. (2010), it is also necessary to correct for the difference between the average extinction of this map and the Brackett- $\gamma$  flux-weighted extinction in the same area. In order to take both effects into account, we calculate the average extinction of the extinction map of Schödel et al. (2010) within the region of the ISO beam and the flux-weighted extinction within the ISO beam

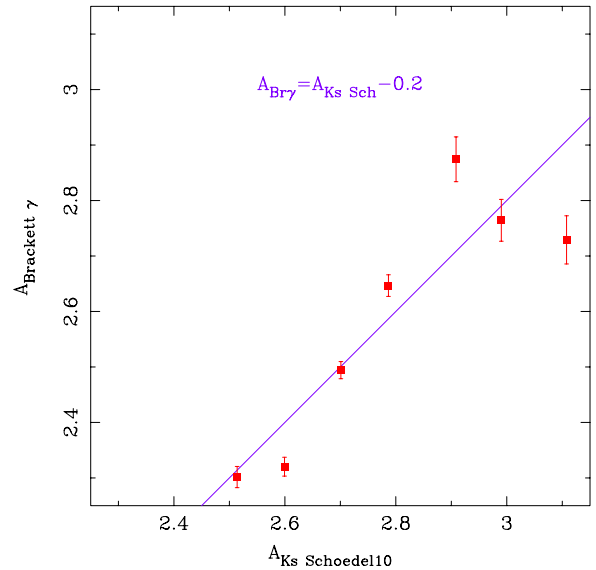


**Figure 7.** Comparison of the extinction derived from our data and that of the  $K_s$  extinction map of Schödel et al. (2010). We bin our data according to the map of Schödel et al. (2010) and measure the extinction in every bin. The error bars show the expected error due to the single pixel SNR. The rms scatter in the plot is 0.1 mag, exceeding the expectation.

(A color version of this figure is available in the online journal.)

for the different line maps. The difference in extinction is small for all lines. We find that the biggest deviation is  $-0.03$  mag for Paschen- $\beta$ , for which line the smallest area was covered, see Figure 5. We apply these corrections to our raw extinction values.

There is an additional bias in integrated extinction measurements that can cause apparent flattening of the extinction law and is especially important for integrated galaxy spectral energy distributions (SEDs) (Calzetti et al. 2000). This bias arises because the measurement of the extinction is flux-weighted, this flux being the observed (extinguished) flux. This creates a problem, because if the extinction is spatially variable, the extinguished flux will be brighter in low-extinction subregions of the image. Thus more weight will be given to these bright, low-extinction subregions of the image. A similar effect of very inhomogeneously distributed extinction in the case of galaxy-integrated measurements (mixed case) is visible in the top left panel of Figure 2 in Calzetti (2001). The effect of this bias is negligible for negligible extinction (i.e., at long wavelengths), but increases toward shorter wavelength together with the extinction, producing an apparent flattening of the measured extinction law. We test and correct for this bias in our measurements, which is in fact small (up to 0.08 mag, see Appendix A).

In the  $H$  band, the hydrogen lines are weaker, both intrinsically as well as being subject to higher extinction. The atmospheric OH lines are also stronger in the  $H$  band. Because of this, only Brackett- $\zeta$  at  $1.736 \mu\text{m}$  is easily detectable, although even this line is polluted by an atmospheric OH line, despite sky subtraction. The structure of this remaining OH-line emission/absorption follows the cubes which are combined to the mosaic and is caused by the time variability of the sky. The sky has to be observed offset from the GC in space and thus also in time due to the brightness of the GC. To correct the sky remnants, we derive OH-line strength maps from the next two strongest OH lines at longer wavelengths and subtract the average of the two maps from the raw Brackett- $\zeta$  map. We scale the subtraction such that any observable structure due to individual cubes in the

**Table 2**  
Average Hydrogen Line Extinction Values Toward the  
Central  $14'' \times 20''$  of the GC

$\lambda$ ( $\mu\text{m}$ )	Extinction
1.282	$7.91 \pm 0.11$
1.736	$4.30 \pm 0.13$
2.166	$2.49 \pm 0.11$
2.625	$1.83 \pm 0.13$
2.758	$1.51 \pm 0.19$
2.873	$1.84 \pm 0.19$
3.039	$2.07 \pm 0.19$
3.297	$1.66 \pm 0.15$
3.74	$1.19 \pm 0.14$
3.819	$1.19 \pm 0.31$
3.907	$1.09 \pm 0.3$
4.052	$1.01 \pm 0.13$
4.376	$1.09 \pm 0.29$
5.128	$0.99 \pm 0.24$
5.908	$1.04 \pm 0.24$
6.772	$0.84 \pm 0.29$
7.459	$0.81 \pm 0.23$
7.502	$0.79 \pm 0.24$
8.76	$2.04 \pm 0.34$
12.371	$1.34 \pm 0.32$
19.062	$1.34 \pm 0.5$

combined cube vanishes. We use the uncertainty of the scaling factor and the difference between the two OH-line maps to estimate the error. In order to further exclude unphysical outliers, we do not use pixels which deviate by more than  $2.5\sigma$  from the median Brackett- $\gamma$ /Brackett- $\zeta$  flux ratio. Integrating over the useful area of both lines, we obtain  $F_{\text{Br}\gamma}/F_{\text{Br}\zeta} = 16.1 \pm 1.3$ . The error due to the OH line subtraction and the pixel selection uncertainty adds an error of 0.081 mag to the extinction for Brackett- $\zeta$ .

For Paschen- $\beta$  we used the smaller area (Figure 5) within its overlap with the central  $14'' \times 20''$ . We use the hydrogen lines detected in the ISO-SWS spectrum (Figure 4) to derive extinction values at the corresponding wavelengths. For the ISO data, which are not spatially resolved, stellar emission could be a problem. We test this by comparing the total Brackett  $\gamma$  from our map with that computed upon declaring stars visible in the line map to be “bad pixels.” The flux difference between the two cases is only 0.04 mag. This contribution, compared to the extinction error of the ISO data of at least 0.14 mag, is therefore not relevant. Since the intrinsic (non-extincted) line ratios follow Case B (Section 4.2), the intrinsic ratios are well known and do not cause an additional error apart from the  $T_e$  uncertainty.

#### 4.3. Extinction Derived

The extinction derived in this analysis is presented in Table 2 and Figure 8. It decreases with wavelength, following a linear relation in this log-log plot between 1.2 and  $2.8 \mu\text{m}$ . At longer wavelengths, the extinction curve changes shape: it contains more bumpy features and is higher than expected from linear extrapolation. For the purpose of investigating the extinction, it is useful to separate the two regimes. Therefore, we define the near-infrared (NIR) as the wavelength regime from 1.2 to  $2.8 \mu\text{m}$  and the mid-infrared (MIR) as the wavelength regime from  $2.8$  to  $26 \mu\text{m}$ . The linear relation within the NIR in the log-log plot implies a power law:

$$A_b = A_a \times (\lambda_a/\lambda_b)^\alpha. \quad (8)$$

**Table 3**  
NIR Infrared Power-law Extinction Fit Parameters

Range Used ( $\mu\text{m}$ )	$A_{\text{Br}\gamma}$	Slope $\alpha$	$\chi^2/\text{dof}$
1.282–2.166	$2.60 \pm 0.11$	$-2.13 \pm 0.08$	2.05/1
2.166–2.758	$2.50 \pm 0.11$	$-1.76 \pm 0.39$	0.54/1
1.282–2.758	$2.62 \pm 0.11$	$-2.11 \pm 0.06$	2.70/3

For the five NIR lines, we obtain  $\alpha = -2.11 \pm 0.06$  and  $A_{\text{Br}\gamma} = 2.62 \pm 0.11$ , see Table 3. The  $\chi^2$  of the fit is 2.70 given three degrees of freedom. Hence, a power law is a good description of the NIR extinction. Since the extinction is obviously grayer beyond  $3.7 \mu\text{m}$ , we test if there is any indication for flattening within the NIR by fitting the red and blue parts of the five NIR lines separately, see Table 3. The slope of the red part, with  $\alpha = -1.76 \pm 0.39$ , is only  $0.9\sigma$  flatter than the blue part. Because this change in slope is not significant, we use the power law obtained from all five NIR lines for deriving the broadband extinction values (Appendix C). The extinction between  $3.7$  and  $8 \mu\text{m}$  is fitted by the following power law:

$$A(\lambda) = (1.01 \pm 0.08) \times (\lambda/4.9 \mu\text{m})^{-0.47 \pm 0.29}.$$

Thus, the MIR extinction is grayer than the NIR extinction.

## 5. DISCUSSION

### 5.1. Comparison with Literature for the GC

We now compare and discuss the extinction curve obtained in this work with the literature.

First of all, we compare with Rieke & Lebofsky (1985), who used mainly data from GC stars to derive the infrared extinction law up to  $13 \mu\text{m}$ . Their finding, however, a single power law of slope  $\approx -1.54$  from  $J$  to  $M$  band, is in contrast with our results. The differences probably lie (1) in their assumption of a universal IR extinction law, whereby  $R_V$  is determined only indirectly, and (2) variability of the stars used. First, for absolute calibration of the extinction law they used  $\sigma$  Sco, which is also detectable in the optical, together with the relation  $E_{V-K}/E_{B-V} = 2.744$  from Schultz & Wiemer (1975) and Sneden et al. (1978). However, this relation was obtained outside of the GC, making their extinction law vulnerable to line-of-sight variations, see Section 5.4. Second, they employ the  $E_{V-M}/E_{B-V}$  of the GC and the bolometric luminosity of IRS7 to estimate  $R_V = A_V/E_{B-V} = 3.09$ . In the process, they use measurements of three stars in the  $M$  band, which is dominated by atmospheric emission, to estimate their lower limit on  $R_V$ . Not only are all of the GC stars used by Rieke & Lebofsky (1985) supergiants, which are in general variable, but variability has, in particular, been reported for IRS7 (Blum et al. 1996). Their indirectly determined  $R_V$  could introduce a systematic error in their extinction measurement. For example, if we reduce  $R_V$  to 2.98 in their calculation, we obtain from their data  $\alpha = -2.04$  between  $J$  and  $K$ . This is compatible with our  $\alpha$ .

In a later work, Rieke (1999) updated Rieke & Lebofsky (1985) using NICMOS data (F110M, F145M, F160W, F222M), again of stars in the GC region. They used spectra of the IRS16 stars (Tamblyn et al. 1996) for deriving absolute extinctions. The extinction curve they found is flatter in “HK” ( $\alpha = -1.58$ ) than in “JH” ( $\alpha = -1.95$ ), in contrast to our extinction law (Section 4.3) and to most other publications which derive a constant slope in the NIR (e.g., Draine 1989). In order to test whether the NICMOS data generally contradict our NIR



extinction law (Section 4.3), we use stars which have NICMOS magnitudes published in Maillard et al. (2004). We use only stars which have been spectroscopically identified as early type (Paumard et al. 2006; Bartko et al. 2009). Early-type stars have colors  $\approx 0$  in the NIR. We exclude IRS13E2 and IRS13E4.0 from the analysis because they are dusty (Fritz et al. 2010). Using the rescaled versions of the extinction map and the  $Ks$ -band magnitudes of Schödel et al. (2010), the NICMOS data are consistent with a single power law with a slope of  $\alpha = -2.16 \pm 0.08$ . Thus, the NICMOS data do not contradict our result of  $\alpha = -2.11 \pm 0.06$  (Section 4.3).

In another study, Viehmann et al. (2005) performed seeing-limited ISAAC  $L$ - and  $M$ -band photometry. Assuming stellar colors they derived a flat extinction slope from  $L$  to  $M$ :  $A_M/A_L = 0.966 \pm 0.05$ . From our NACO broadband extinction values (Appendix C), we obtain a consistent value:  $A_M/A_L = 0.88 \pm 0.23$ . However, these results are not directly comparable, because Viehmann et al. (2005) used a narrow  $M$  band with a FWHM =  $0.10 \mu\text{m}$  at  $4.66 \mu\text{m}$ . At this wavelength, a CO absorption feature is visible in the ISO spectra (Lutz et al. 1996; Moneti et al. 2001), see Figure 8.

Scoville et al. (2003) obtained an absolute extinction map of the GC for Paschen- $\alpha$ . To do this, they used NICMOS narrowband imaging at Paschen- $\alpha$  ( $1.87 \mu\text{m}$ ) and at  $1.90 \mu\text{m}$  to construct the line map. They took a VLA continuum map at 6 cm to use as extinction-free data. Using their extinction map, we compute an average extinction of  $A_{\text{Pa}\alpha} = 3.54$  integrated over the ISO beam. This value is consistent with our value of  $A_{\text{Pa}\alpha} = 3.56 \pm 0.11$ , obtained from the best-fit power law.

Schödel et al. (2010) measured the extinction toward the GC using NACO data in  $H$ ,  $Ks$ , and  $L'$  bands. By comparing the magnitude of the peak of the luminosity function (the red clump) with its expected magnitude, they obtained the total light modulus of the GC. They then used a distance to the GC of  $8.03 \pm 0.15$  kpc, derived from different works, to obtain the extinction:  $A_H = 4.48 \pm 0.13$ ,  $A_{Ks} = 2.54 \pm 0.12$ , and  $A_{L'} = 1.27 \pm 0.18$ .

Schödel et al. (2010) also derived the selective extinction  $E_{H-Ks} = (A_H - A_{Ks})/A_{Ks}$  from the red clump extinction values. They then used  $E_{H-Ks}$  for obtaining a  $Ks$ -band extinction map from the observed stellar colors. Surprisingly, the average of the map is, with  $A_{Ks} = 2.70$ , larger than the extinction obtained from the red clump. It can be seen from Table A.2 in Schödel et al. (2010) that most individual stars have larger values of  $H - Ks$  than the stellar population of the red clump in the luminosity function, the reason for which is not clear.

We do not know which of the two Schödel et al. (2010) extinction values should be preferred. Because of this, we use the average and enlarge the error by adding  $\sqrt{1/2} \times (A_{Ks1} - A_{Ks2}) = 0.11$  mag. We obtain  $A_{Ks} = 2.62 \pm 0.16$  for the full field of Schödel et al. (2010). Their extinction map has an average of  $A_{Ks} = 2.70$  over the full map. However, the average is  $A_{Ks} = 2.68$  over the ISO field of view. Therefore, we correct the average by multiplying with  $2.68/2.70$  and obtain  $A_{Ks} = 2.60 \pm 0.16$  as a final value for comparison with our extinction.

The issue of two possible extinction values in the  $Ks$  band also extends to the other bands. We assume a linear scaling of the extinction values based on stellar colors with the extinction values derived from the red clump in each band. We again use the average of red clump extinction and the selective extinction. We obtain  $A_H = 4.58 \pm 0.24$  and  $A_{L'} = 1.30 \pm 0.19$  as final values for comparison with our extinction values.

**Table 4**  
Error Sources for the Extinction

Error Source	$\Delta\text{mag}$ for Brackett $\gamma$	$\Delta\text{mag}$ for Other Lines
• IR calibration error and line S/N	0.073	0.073–0.50
• Electron temperature	0.043	0.043
• Selection of good pixels in Brackett- $\gamma$	0.03	0.03
• Scatter comparing with Schödel et al. (2010)	0.07	0.07
• Selection of good pixels in other lines	0	0–0.088
Total	0.114	0.114–0.507

If we now compare with our broadband extinction values (see Appendix C), we obtain the following differences between our results and Schödel et al. (2010):  $A_{H \text{ lines}} - A_{H \text{ Sch}} = 0.07 \pm 0.25$ ,  $A_{Ks \text{ lines}} - A_{Ks \text{ Sch}} = 0.07 \pm 0.17$ , and  $A_{L' \text{ lines}} - A_{L' \text{ Sch}} = -0.10 \pm 0.23$ . For the calculation of the errors here, we exclude the zero-point errors in the  $H$  and  $Ks$  bands because both results use the same calibration data, and we also exclude the error due to  $R_0$  because we use the differences to measure  $R_0$ , see Section 5.2. To summarize, our values are all consistent with the values of Schödel et al. (2010).

In Table 4, we present the various sources of error for our extinction values. Our data are well fitted with a power law in the NIR ( $\chi^2/\text{dof} = 0.71$ ), see Section 4.3 as expected from the established literature (Cardelli et al. 1989). An error in the radio data (such as an error on  $T_e$ ) affects all values in the same way, such that its influence on the  $\chi^2$  of the power-law fit is much smaller than the influence of independent errors in the NIR data. Because the power law does not continue to the MIR till negligible extinction in our data, it is not possible to obtain the absolute extinction independent of the radio data, as was done in Landini et al. (1984). However, the value for  $T_e$  which we use is consistent with both Roberts & Goss (1993) and Shukla et al. (2004). Therefore, it is unlikely that there is a relevant systematic error in the extinction due to the radio data.

## 5.2. A Photometric Distance to the GC

The distance to the GC  $R_0$  is used to derive distances to all but the closest regions of the Galaxy and is one of the fundamental parameters for building Milky Way models. Knowing  $R_0$  is hence of general relevance. Prior to this publication there was no reliable measurement for the GC extinction that was independent of  $R_0$ . Works that did derive  $R_0$  photometrically (Nishiyama et al. 2006b; Groenewegen et al. 2008; Dambis 2009; Matsunaga et al. 2009) used stars in the bulge, not directly in the GC. On the other hand, stars directly in the GC have been used to derive  $R_0$  from the dynamics of their stellar orbits around the supermassive black hole (Eisenhauer et al. 2003a; Ghez et al. 2008; Gillessen et al. 2009), and by using the statistical parallax of the population of late-type stars in the GC (Genzel et al. 2000; Trippe et al. 2008).

With our extinction measurement we can obtain a photometric  $R_0$  from stars in the GC. We combine our extinction measurement with the extinction measurement of Schödel et al. (2010). These authors obtained the total luminosity modulus of the red clump stars in the GC. Because the luminosity modulus involves both the extinction and the distance modulus it was necessary for Schödel et al. (2010) to assume a distance for calculating



extinction values, for which they used  $R_0 = 8.03 \pm 0.15$  kpc. Here, we can use the extinction differences between the two works, see Section 5.1 in order to estimate  $R_0$ . For the  $Ks$  band, we obtain  $R_0 = 7.78 \pm 0.63$  kpc. From the  $H$  band we obtain  $R_0 = 7.78 \pm 0.95$  kpc, and from the  $L'$  band we obtain  $R_0 = 8.41 \pm 0.94$  kpc. The errors follow from the errors of the extinction differences between our extinction values and those of Schödel et al. (2010), see Section 5.1. We use the weighted average of all values as our final value:  $R_0 = 7.94 \pm 0.65$  kpc. For the error we use the smallest single error, the relative error of  $Ks$  band, because the errors are correlated between the filters.

Nishiyama et al. (2006b) used red clump stars in the inner bulge to derive a photometric distance and obtained  $R_0 = 7.52 \pm 0.36$  kpc. Our value is about  $0.6\sigma$  larger. Since in both works the same absolute red clump magnitude is used, the consistency indicates only that other uncertainties (like the extinction) are not larger than assumed. However, it is still possible that the absolute magnitude has a bigger error than assumed. Our result is also consistent with the review of Reid (1993), who determined  $R_0 = 8.0 \pm 0.5$  kpc, and the recent review of Genzel et al. (2010), who determined  $R_0 = 8.15 \pm 0.14 \pm 0.35$  kpc from direct and indirect measurements, and  $R_0 = 8.23 \pm 0.2 \pm 0.19$  kpc from only direct measurements.

Conversely, assuming that the direct estimate of  $R_0$  by Genzel et al. (2010) is correct we can test the red clump magnitude. The red clump in the GC has then a magnitude of  $M_{Ks} = -1.59 \pm 0.13$ . The value used by us and Schödel et al. (2010) is  $M_{Ks} = -1.47$ , and the two values are consistent, although the GC star formation history (Blum et al. 2003; O. Pfuhl et al. 2011, in preparation) and metallicity (Cunha et al. 2007) were not modeled to obtain  $M_{Ks}$ . Therefore, as expected according to Salaris & Girardi (2002),  $M_{Ks}$  of the red clump is relatively independent of the star formation history and metallicity and thus is a reliable distance indicator.

### 5.3. Spatial Distribution of the Extinction and the Extinction Toward Sgr A\*

Our data do not have enough S/N to obtain a good extinction map. However, because our absolute values for the extinction are more accurate than the extinction of Schödel et al. (2010), combining our absolute value and the extinction map of Schödel et al. (2010) is useful. For this, we adjust the extinction map of Schödel et al. (2010) such that in it the extinction is the same as our interpolated  $A_{Br\gamma}$  of the same area. This means that we multiply the map of Schödel et al. (2010) by 0.976.

From the adjusted map, we use  $A_{Br\gamma}$  toward Sgr A\* to derive broadband extinctions (Appendix C) of  $A_H = 4.21 \pm 0.10$ ,  $A_{Ks} = 2.42 \pm 0.10$ , and  $A_{L'} = 1.09 \pm 0.13$ . Effectively, this is the extinction to the stars with  $r \leq 0''.5$  around Sgr A\* due to the procedure used by Schödel et al. (2010). However, it is adjusted for the SED difference between stars and Sgr A\* (Appendix C).

The light that reaches Earth from the GC crosses many regions of the Galaxy. It is possible that dust associated with the minispiral extincts the light in the GC itself. However, because the extinction derived from the minispiral is consistent with the extinction derived from stars of Schödel et al. (2010), the extinction must occur mainly in front of the GC. For testing this further, we smooth the Brackett- $\gamma$  flux to the resolution of the extinction map of Schödel et al. (2010). This we compare with the extinction map of Schödel et al. (2010) in bins defined by the smoothed minispiral flux. We do not find a correlation between the minispiral flux and the extinction derived from stars. Furthermore, the scatter of the median extinction is only

0.04 mag over the different flux means. In addition, the small far-infrared flux (Becklin et al. 1982; Guesten et al. 1987) of the central few parsecs shows that hardly any UV radiation is absorbed there (Brown & Liszt 1984). All in all, the NIR extinction must be very small (at least  $A_{Ks} < 0.1$ ) inside the central parsec.

In order to further constrain the location of the extinction in the line of sight, we use the  $H - Ks$  values of the stars in Table A.2 of Schödel et al. (2010). Since the intrinsic color  $|H - Ks| < 0.2$  for nearly all stars, the  $H - Ks$  of each star depends nearly only on the extinction. We then measure how many stars in the table have an  $H - Ks$  compatible with zero extinction. Thereby, we exclude stars which are so blue and faint in  $Ks$  that they would be too faint for detection if they were to have the extinction of the GC. We exclude them in order to avoid a bias toward foreground stars. After this, we obtain that only five of 6324 stars have an  $H - Ks$  color compatible with zero extinction. According to Philipp et al. (1999), the Galactic disk and bulge (outside of 300 pc) have 2.3% of the flux of the GC at  $r = 10''$ .<sup>6</sup> Because the ratio of extinction-free stars to all stars of 0.1% is much smaller than the flux contribution of Galactic bulge and disk to the flux in the center of 2.3%, there must be extinction within the Galactic disk. We then measure up to which extinction it is necessary to include stars in order to account for the 2.3% star contribution of Galactic disk and bulge. We find that it is necessary to include stars with extinction up  $A_{Ks} = 2.0$ . This is about 3/4 of the total extinction toward the GC.

Therefore, the measured extinction is mainly not associated with the giant molecular clouds in the Nuclear bulge (Mezger et al. 1996) and as such is not related to special processes in the central 50 pc. Because most bulges do not contain a lot of dust, it is likely that most of the extinction is caused by dust in the Galactic disk. As a result, the measured extinction curve is likely a typical extinction curve of dust in the Galactic disk.

The extinction toward the GC is higher than the average extinction of the bulge behind the Galactic plane (Marshall et al. 2006). However, there are also regions with much higher extinction close to the GC (Ramírez et al. 2008). Therefore, the extinction of the GC is not exceptional for an 8 kpc view through the Galactic disk.

### 5.4. The NIR Extinction

Our NIR data can be well fitted with a power law of  $\alpha = -2.11 \pm 0.06$  ( $\chi^2/\text{dof} = 2.70/3$ ). This strengthens the case for the use of a power law as model for the extinction in the NIR (e.g., Cardelli et al. 1989). Our slope is steeper than the slope of  $\alpha \approx -1.75$  of most reviews see, e.g., Savage & Mathis (1979), Mathis (1990), and Draine (2003). However, most of the measurements (e.g., Schultz & Wiemer 1975; Landini et al. 1984; Whittet 1988; He et al. 1995) combined in these reviews used relatively few stars; these stars are detectable in the optical and partly also in the UV, have  $A_V \leq 5$ , and are mostly closer than 3 kpc, see, e.g., He et al. (1995). The extinction measurement of Rieke & Lebofsky (1985) toward the GC was also tied partly to measurements of stars which are visible also in the optical.

Since about 2005, large infrared surveys have become available and are now used by most publications about extinction.

<sup>6</sup> We exclude the central  $10''$  because there the total flux is dominated by young stars. Since there are only a few young stars due to the top-heavy initial mass function (Bartko et al. 2010) they are irrelevant for the star number ratio.

**Table 5**  
NIR Infrared Extinction Law from Literature

Publication	$E_{J-H}/E_{H-K}$	Slope $\alpha$
Indebetouw et al. (2005)		$-1.65 \pm 0.12$
Messineo et al. (2005)		$-1.9 \pm 0.1$
Nishiyama et al. (2006a)		$-1.99 \pm 0.08$
Straizys & Laugalys (2008)	$2 \pm 0.13$	$-2.07 \pm 0.23$
Gosling et al. (2009)		$-2.64 \pm 0.52$
Nishiyama et al. (2009)	$2.09 \pm 0.13$	$-2.23 \pm 0.23$
Stead & Hoare (2009)		$-2.14 \pm 0.045$
Zasowski et al. (2009)	$2.11 \pm 0.1$	$-2.26 \pm 0.17$
Schödel et al. (2010)		$-2.21 \pm 0.24$
Our work		$-2.11 \pm 0.06$
Weighted average		$-2.07 \pm 0.16$

**Notes.** NIR extinction slope measurements of diffuse ISM extinction since 2005. When  $\alpha$  is not given in the publication, or the effective wavelength is unusual we calculate  $\alpha$  from  $E_{J-H}/E_{H-K}$ . Thereby we use for  $\lambda'_{\text{eff}}$  the wavelength 1.24, 1.664, and 2.164  $\mu\text{m}$  (Nishiyama et al. 2009). The error is either the measurement error in the publication or the scatter of different sight lines. From Nishiyama et al. (2009), we only use the 2MASS data, since the SIRIUS data are identical to Nishiyama et al. (2006a). We use all values for the calculation of the weighted average.

Since now no detection in the optical is necessary, and because it is easier to characterize high extinction, many publications (see Table 5) measured the extinction toward the highly extinguished inner Galactic disk and bulge, at about 8 kpc distance. Most of these publications measure  $\alpha \approx -2.1$ .

It is possible that the change in the measured  $\alpha$  around 2005 is due to systematic errors. Stead & Hoare (2009), for example, suggested that the use of the isophotal wavelength instead of the effective wavelength caused the flatter slope in the measurement prior to 2005. We think, however, that it is unlikely that errors in the effective wavelengths are the reason for the discrepancy: while it is correct that using the isophotal filter wavelengths can lead to errors in  $\alpha$ , using the effective wavelength as presented in Stead & Hoare (2009) overestimates  $\alpha$  slightly, see Appendix D. Furthermore, even if the isophotal wavelength is used, the systematic error on  $\alpha$  is at maximum 0.07 for the hot stars (see Appendix D for a 9480 K star) used in most works before 2005. Additionally, Fitzpatrick (2004) used Two Micron All Sky Survey (2MASS) data of solar neighborhood stars and, using the effective wavelength, obtained  $\alpha \approx -1.84$ .

Since the dust probed by studies which obtain  $\alpha \approx -1.75$  and  $\alpha \approx -2.1$ , respectively, is not identical it seems likely that the extinction law varies between these regions. A strong piece of evidence for truly variable extinction is the correlation of  $R_V$  with  $\alpha$  in Fitzpatrick & Massa (2009), whereas for the standard  $R_V = 3.1$   $\alpha = -1.77 \pm 0.05$ . This work used 14 stars with observations from 120 nm to  $Ks$  band. All in all, we think it is likely that there is a transition of a mostly flatter NIR extinction in the solar neighborhood to a steeper one in most parts of the Galactic disk. Naturally, further tests of the NIR extinction slope variation via measurement of the NIR extinction slope in the local low-extinction sight lines, and in the Galactic disk, using the best methods available today would be very valuable.

For most molecular clouds, the extinction is, with  $\alpha \approx -1.8$  (Román-Zúñiga et al. 2007; Naoi et al. 2006; Kenyon et al. 1998; Flaherty et al. 2007; Lombardi et al. 2006), flatter than for the Galactic disk sight lines. However, there are also clouds with deviating  $\alpha$ , with an  $\alpha$  range from  $-1$  to  $-2.4$  (Froebrich & del Burgo 2006; Whittet 1988; Racca et al. 2002; Naoi et al. 2007).

There are some features typical of molecular clouds that are visible in the ISO-SWS spectrum. Whittet et al. (1997) determined that about a third of the extinction toward the GC is caused by molecular clouds with substructure and the rest by diffuse extinction. A relatively small contribution of the extinction by molecular clouds is also supported by the fact that the extinction variation toward the central parsec is less than one-third of the maximum extinction, as can be seen in the extinction map of Schödel et al. (2010). This means also that the molecular cloud contribution is not visible in terms of star counts as it is in the case of, e.g., the Coalsack. Accordingly, the line of sight toward the GC is not dominated by molecular cloud extinction. Thus, we exclude molecular cloud extinction in our quantitative comparison with the GC.

For comparison, we use publications about the extinction toward the Galactic disk and bulge. In practice, this means only publications since 2005, see Table 5. We use these data for calculating the weighted average:  $\alpha = -2.07 \pm 0.16$ . Of these nine publications used, only Indebetouw et al. (2005) are inconsistent with the others. Hence, the extinction law is likely constant toward the inner Galactic disk and bulge and can probably also be used for other fields in that region.

Due to the high absolute extinction in the inner Galactic disk, this region contributes more to the global extinction of the Galaxy than the solar neighborhood or the halo of the Galaxy (Schlafly et al. 2010). Therefore, the steeper extinction law in the NIR of the inner Galactic disk is probably more important when integrated over the volume of the Milky Way. Similarly, for other galaxies for which our Galaxy is typical, a steeper extinction law could also be more important.

### 5.5. The Optical Extinction

Rieke et al. (1989) estimated an optical extinction of  $A_V = 31$  toward the GC using the extinction law of Rieke & Lebofsky (1985). The GC is, due to this high extinction, undetectable in the optical. As a result, any estimate of  $A_V$  for the GC is indirect. Since both this paper and Schödel et al. (2010) obtain a different infrared extinction law to Rieke & Lebofsky (1985), it seems possible that the optical extinction toward the GC is also different from the one assumed in Rieke & Lebofsky (1985).

In order to test this, we use data which have a more direct connection to the GC than  $\sigma$  Sco which was used by Rieke & Lebofsky (1985). The shortest wavelength at which the GC has been observed is the  $z$  band (Henry et al. 1984; Rosa et al. 1992; Liu et al. 1993). In order to estimate the  $z$ -band extinction, we use the magnitudes of the IRS16 stars from these works, because these stars and their intrinsic colors are well known. We neglect the data for IRS16C in Liu et al. (1993) because the star is brighter in this work compared to all other works. We use the extinction map and the IRS16 magnitudes of Schödel et al. (2010) in order to calculate the dereddened  $Ks$ -band magnitudes of the IRS16 stars. We then subtract the dereddened  $Ks$ -band magnitudes and an intrinsic color of  $z - Ks = -0.25$  from the measured  $z$ -band magnitudes of IRS16 to obtain  $z$ -band extinctions.

We convert the  $z$ -band extinctions into an extinction power law between Paschen- $\beta$  and the true effective wavelength for extinction measurements ( $\lambda_{\text{true}}$ ) of the GC (see Appendix D). In the case of Henry et al. (1984) and Liu et al. (1993), the wavelengths given in the publications are probably  $\lambda_{\text{true}}$ . We assign to them an error of 0.01  $\mu\text{m}$ . Rosa et al. (1992) give the central wavelength for stars extinguished by GC extinction and unextinguished stars. Since both are incorrect, see Appendix D,

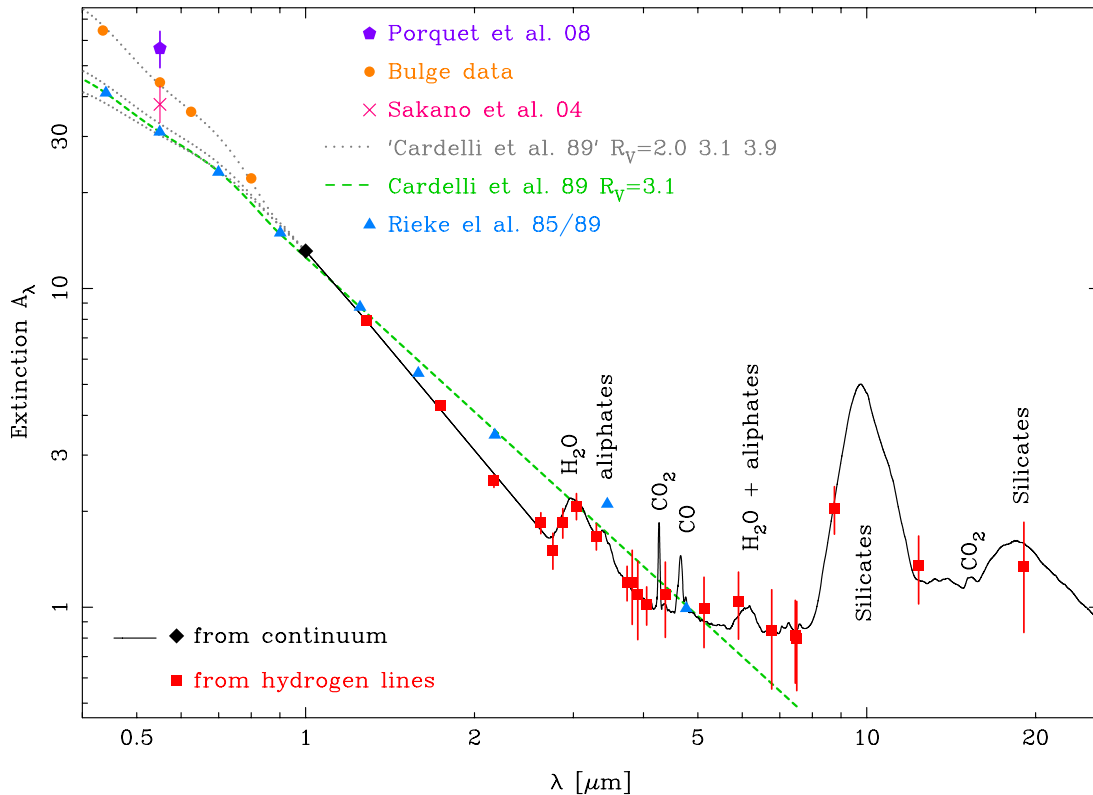


**Figure 8.** Extinction toward the central  $14'' \times 20''$  of the GC. We use hydrogen lines for obtaining the extinction between  $1.28$  and  $18 \mu\text{m}$  (red boxes) and stellar colors for  $1 \mu\text{m}$  (black diamond). We interpolate the data by use of the continuum emission (black line). The spectral resolution of the interpolation is not high enough to resolve all features like the CO feature at  $4.7 \mu\text{m}$  fully. We mark the larger extinction features (Lutz et al. 1996; Chiar et al. 2000). We use the central bulge data of Sumi (2004), Nishiyama et al. (2008), and Revnivtsev et al. (2010) for extending the extinction curve to the visible (orange dots). For comparison we add a value for  $A_V$  derived from the X-ray spectrum of Sgr A\* (Porquet et al. 2008; violet pentagon). In the same way we use the gas in front of Sgr A East (Sakano et al. 2004; pink cross). The extinction curve differs from Rieke & Lebofsky (1985) and Rieke et al. (1989) (blue triangles), the results of which are only partly based on GC data. The GC data differ also from the Cardelli et al. (1989) curve (fitted to  $R_V = 3.1$  observations; green dashed line). The optical extinction toward the GC is uncertain. We use three curves of the type used by Cardelli et al. (1989) with  $R_V = 2.3, 3.1, 3.9$  (dotted gray lines from top down) for showing the possible range. (A color version of this figure is available in the online journal.)

we calculate from the given central wavelength and FWHM of the optical system  $\lambda_{\text{true}} = 0.97 \mu\text{m}$ . Due to the additional uncertainties in calculating the effective wavelength, we assume an error of  $0.015 \mu\text{m}$ . The effective wavelength uncertainty and the scatter of the IRS16 stars are used for the calculation of the errors.

In this way, we obtain  $\alpha = 1.99 \pm 0.09$ ,  $\alpha = 1.91 \pm 0.14$ , and  $\alpha = 2.165 \pm 0.13$  from Henry et al. (1984), Rosa et al. (1992), and Liu et al. (1993). The average slope is, with  $\alpha = -2.02 \pm 0.07$ , consistent with our determined NIR slope of  $\alpha = 2.11 \pm 0.06$  (Section 4.3). Using the average of the three Paschen- $\beta$   $z$  slopes, we obtain  $A_{1 \mu\text{m}} = 13.11 \pm 0.30$ . This extinction is slightly higher than interpolating Rieke et al. (1989) although our  $K$ -band extinction is smaller, see Figure 8.

We now consider how the  $z$ -band extinction should be extrapolated into the optical. Molecular cloud features are probably responsible for a third of the extinction toward the GC, see Section 5.3. An above average contribution of molecular cloud extinction to the GC is also supported by the fact that the extinction toward the GC is higher than the average bulge extinction (Section 5.3). If we assume a high  $R_V = 5.5$  for the molecular cloud extinction and  $3.1$  for the other two thirds, the average  $R_V \approx 3.9$  for the GC. Using a Cardelli et al. (1989) curve with this  $R_V$  (but with  $\alpha = -1.85$  between  $0.91 \mu\text{m}$  and  $1 \mu\text{m}$  for reducing the jumps in the slope) to extrapolate to the optical, we obtain  $A_{\lambda=0.55 \mu\text{m}} = 30.3$ .

However, most molecular clouds do not have an  $R_V$  of  $5.5$ . Thus, even assuming that one-third is caused by molecular cloud extinction and two thirds by normal extinction, the real  $R_V$  is probably closer to  $3.1$ . In addition, the high strength of aliphate ( $3.4 \mu\text{m}$ ) and silicate ( $9.7 \mu\text{m}$ ) features is different from the extinction in molecular clouds (Section 5.6). These features are even stronger than in most diffuse extinction sight lines. Furthermore the steep NIR extinction slope of  $\alpha = -2.11$  is not typical of molecular cloud extinction (Section 5.4). Therefore, we obtain another estimate, extrapolating to the visible also with the normal  $R_V = 3.1$  (using  $\alpha = -1.95$  between  $0.91 \mu\text{m}$  and  $1 \mu\text{m}$ ). In this case, we obtain  $A_{\lambda=0.55 \mu\text{m}} = 33$ .

A much steeper extinction law than the standard  $R_V = 3.1$  from  $B$  band to  $J$  band is measured (Udalski 2003; Sumi 2004; Revnivtsev et al. 2010; Nishiyama et al. 2008) toward parts of the bulge which have a much smaller extinction than the GC ( $A_V < 7$  in the case of Nishiyama et al. 2008). In particular, Nishiyama et al. (2008) measured  $A_V/A_J = 5.32 \pm 0.14$ , while according to Rieke & Lebofsky (1985)  $A_V/A_J = 3.55 \pm 0.16$  for the standard  $R_V = 3.1$ . We fit these bulge data points with a Cardelli et al. (1989) curve with  $R_V = 2.0$  (using  $\alpha = -2.02$  between  $0.91 \mu\text{m}$  and  $1 \mu\text{m}$ ). Extrapolating the  $z$ -band extinction of the GC with this curve, we obtain  $A_{\lambda=0.55 \mu\text{m}} = 44$ . The aliphate and silicate features toward the GC are stronger than in diffuse extinction, while they are even weaker in molecular cloud extinction, see Section 5.6. This means that the strength of



these features is anticorrelated with  $R_V$  for  $3.1 \leq R_V \leq 5.5$ . Extrapolating this anticorrelation to the stronger feature toward the GC implies that  $R_V < 3.1$  toward the GC, which in turn implies an  $A_V > 33$ .

Figure 4 in Fitzpatrick & Massa (2009) shows a correlation between the infrared power-law slope  $\alpha$  and  $R_V$ . The correlation implies that the slope in the infrared approximately continues into the red. Using a second-order polynomial to fit their 13 measurements (neglecting one outlier), we obtain  $R_V = 2.48 \pm 0.06$  for the GC, using our measurement of  $\alpha = -2.11 \pm 0.06$  in the GC. Thus, because a small  $R_V$  implies a high  $A_V$ , this again implies that the optical extinction toward the GC is probably large.

X-rays can shed further light on  $A_V$ . X-ray photons, for example, are attenuated by scattering and absorption which are related to the extinction (Morrison & McCammon 1983; Predehl & Schmitt 1995). At the energy at which the GC is observed ( $\approx 3$ –8 keV), absorption by astronomical metals is much stronger than scattering by dust grains (Predehl & Schmitt 1995; Porquet et al. 2008). For the absorption the chemical state of the absorbing material is irrelevant and depends only on the integrated column density of astronomical metals. Thus the X-ray absorption can be used to constrain dust models and the extinction.

Here we investigate the implications only for the extinction. Observationally, the X-ray absorption is well correlated with  $A_V$  (Predehl & Schmitt 1995) in most Galactic sight lines. However, there are active galactic nuclei with different X-ray absorption to  $A_V$  ratios (Maiolino et al. 2001; Li 2007). Toward Sgr A\* we obtain a column density of  $N_H = 10.5 \pm 1.4 \times 10^{22} \text{ cm}^{-2}$ , averaging over the different states (Porquet et al. 2008). Thereby we assume an intrinsic X-ray power law for the flares of Sgr A\* (Dodds-Eden et al. 2009). We thus obtain an X-ray derived  $A_V = 56.7 \pm 7.4$  for the GC (Figure 8) using the  $N_H/A_V$  relation of Predehl & Schmitt (1995). Using UV-derived  $N_H/A_V$  relations (Bohlin et al. 1978; Draine 1989; Zubko et al. 2004), we obtain  $A_V$  from 53 to 59. Our best-fitting dust model (Section 5.8) gives  $A_V \approx 48$  for the measured  $N_H$ .

There is the possibility that part of the column density toward Sgr A\* arises in ionized gas in the halo of the supernova remnant Sgr A East (Maeda et al. 2002; Porquet et al. 2008), in which case not all of the  $N_H$  (measured by X-rays) toward Sgr A\* is caused by dust. For example, Sakano et al. (2004) measured an  $N_H = 15 \times 10^{22} \text{ cm}^{-2}$  for hot plasma, and  $N_H = 7 \times 10^{22} \text{ cm}^{-2}$  for somewhat colder plasma of Sgr A East. The second value is perhaps typical of plasma lying in the line of sight to Sgr A\*. Accordingly, it is possible that the column toward the colder plasma corresponds to the column to Sgr A\*. If this is the case, we obtain a lower  $A_V = 37.8$ , using the relation of Predehl & Schmitt (1995). However, probably the foreground extinction toward Sgr A East and Sgr A\* is not fully homogeneous. In principle, it is possible to obtain a better  $N_H$  toward the Sgr A region by measuring  $N_H$  toward point sources outside of Sgr A East. By comparing such a map with an IR excess map, it should be possible to obtain a better estimate for  $N_H$  for the GC.

Overall, the evidence for an  $R_V < 3.1$  is slightly larger than for  $R_V > 3.1$ , which means that  $A_{\lambda=0.55 \mu\text{m}} > 33$ . However, it is clear that only a direct measurement in the visible can clarify the value of  $R_V$ . The GC extinction attenuates 16NW, the brightest blue star in the GC with unextinguished  $m_V \approx 5.5$ , to a magnitude of  $m_V = 34$ –43 depending on  $R_V$  (since this simulated measurement integrates over the V band the extinctions are smaller than the corresponding  $0.55 \mu\text{m}$  extinctions).

## 5.6. The MIR Extinction

At wavelengths  $> 2.8 \mu\text{m}$  extinction features are visible in the ISO-SWS spectrum, even shortward of the deep silicate feature at  $9.7 \mu\text{m}$  (Figure 4). These features are known from Butchart et al. (1986), Willner et al. (1979), Lutz et al. (1996), and Chiar et al. (2000).

Most of these features are caused by ices like the  $\text{H}_2\text{O}$  feature at  $3.1 \mu\text{m}$  (Butchart et al. 1986; Lutz et al. 1996; Chiar et al. 2000) and the  $\text{CO}_2$  feature at  $4.3 \mu\text{m}$  (Lutz et al. 1996; de Graauw et al. 1996b). Among others, Whittet et al. (1988), Rosenthal et al. (2000), and Knez et al. (2005) detected these features in many other sight lines with different strengths, both compared to one other as well as to the continuum extinction. Rawlings et al. (2003) and Whittet et al. (1997) did not detect  $\text{H}_2\text{O}$  ice in sight lines consisting of diffuse interstellar material with  $A_V \approx 10$ . Thus, these features are likely only visible in sight lines through molecular clouds and not in purely diffuse extinction regions (Whittet et al. 1997; Chiar et al. 2000). This view is supported by the CO clouds in the Galactic arms in front of the GC (Sutton et al. 1990). This CO is also visible in the ISO-SWS spectrum (Lutz et al. 1996; Moneti et al. 2001). The detection of molecular cloud features toward the GC is not unique, ice features are also detected toward the Quintuplet cluster at a distance of about  $12'$  to the GC, where they are slightly weaker compared to the continuum extinction (Chiar et al. 2000).

Other extinction features, like the strong aliphatic hydrocarbon feature at  $3.4 \mu\text{m}$  (Willner et al. 1979), are caused by diffuse dust and are thus a general visible feature of extinction (Chiar et al. 2000; Rawlings et al. 2003). The feature at  $3.4 \mu\text{m}$  is about a factor of two stronger toward the GC than in the local diffuse extinction (Rawlings et al. 2003; Gao et al. 2010). The  $3.4 \mu\text{m}$  feature is typical for diffuse dust. In molecular clouds it is not detected (Pendleton & Allamandola 2002).

In order to better constrain the shape of the extinction curve, we use the continuum of the ISO-SWS spectrum, see Appendix B and Figure 8.

For the silicate feature at  $9.7 \mu\text{m}$ , we obtain an optical depth of  $\Delta\tau_{\text{Si}9.7} = 3.84 \pm 0.52$  relative to the continuum at  $7 \mu\text{m}$  from our interpolated extinction curve. The depth is similar to that obtained by Chiar et al. (2000) of  $\Delta\tau_{\text{Si}9.7} = 3.46$  and by Roche & Aitken (1985) of  $\tau_{\text{Si}9.7} = 3.6$ . According to van Breemen et al. (2010), the shape of  $9.7 \mu\text{m}$  silicate feature of the GC is identical to sight lines with diffuse extinction and slightly different to sight lines with molecular clouds. Using our broadband extinction values (Appendix C), we obtain  $\Delta\tau_{\text{Si}9.7}/E(J-K) = 0.70 \pm 0.10$ , consistent with Roche & Aitken (1985). This is more than the value of  $\Delta\tau_{\text{Si}9.7}/E(J-K) = 0.34$  in nearly all other diffuse sight lines (Roche & Aitken 1984; van Breemen et al. 2010). Sight lines with molecular clouds also have  $\tau_{\text{Si}9.7}/E(J-K) = 0.34$  or even smaller values (van Breemen et al. 2010). The large  $\Delta\tau_{\text{Si}9.7}/E(J-K)$  toward the GC is probably caused by an abnormally high  $\Delta\tau_{\text{Si}9.7}$ . A larger silicate dust to carbon dust ratio in the inner Galaxy compared to the local diffuse medium (Roche & Aitken 1985; van Breemen et al. 2010) could explain the high  $\Delta\tau_{\text{Si}9.7}/E(J-K)$  toward the GC. With a higher silicate abundance  $\Delta\tau_{3.4 \mu\text{m}}/E(J-K)$  toward the GC should be identical to the local value. However, it is twice the local value. Porous dust grains cause both a strong  $3.4 \mu\text{m}$  and a strong  $9.7 \mu\text{m}$  feature (Gao et al. 2010). Porosity is also one element of the dust model of Zubko et al. (2004), which best fits our continuum extinction data, see Section 5.8.

In the continuum, CO<sub>2</sub> is visible at 15  $\mu$ m (Gerakines et al. 1999). It is, however, much weaker than in the observations of extinction in molecular clouds observed by Knez et al. (2005). In contrast, the silicate feature at 18  $\mu$ m toward the GC is much stronger than the CO<sub>2</sub> feature, see Figure 8.

Rieke & Lebofsky (1985) and Rosenthal et al. (2000) can fit all their extinction values up to 7.5  $\mu$ m with a single power law. This single power-law extinction is inconsistent with the flattening of the extinction curve in our data at around 4  $\mu$ m, see Section 4.3. In the continuum, there are no strong extinction features apparent between 3.7 and 8  $\mu$ m, see Figure 8. Some weak features due to H<sub>2</sub>O, NH<sub>3</sub>, CO<sub>2</sub>, HCOOH, and aliphatic hydrocarbon are tentatively identified by Lutz et al. (1996) and Chiar et al. (2000). All the features are weaker than  $\tau = 0.15$ . Thus, these features are too weak to explain a significant part of the extinction difference between the measured extinction and a single power law. There is some indication for a steeper slope around 3.9  $\mu$ m and a flatter one at longer wavelengths. Also, the data of Nishiyama et al. (2009) and most theoretical models (Section 5.8) exhibit a smooth flattening in the transition region.

Zasowski et al. (2009), Jiang et al. (2003, 2006), Gao et al. (2009), Flaherty et al. (2007), Román-Zúñiga et al. (2007), Nishiyama et al. (2009), and Indebetouw et al. (2005) also detected a flattening of the extinction at MIR wavelengths toward different regions of the Galaxy. Some of these observations, such as Nishiyama et al. (2009) and Zasowski et al. (2009), targeted diffuse extinction in the bulge and the Galactic disk. Therefore, the flattening of the curve in the MIR is not caused by the molecular cloud in front of the GC.

The extinction curves of other galaxies in the MIR are more difficult to interpret, because the extinction in other galaxies is not likely to be caused by an uniform foreground screen. However, since a mixed model (Förster Schreiber et al. 2001) produces a flattening of the extinction curve at higher extinction, while in the GC a flattening at smaller extinction is observed, it is still possible to find qualitative signs for the GC extinction curve in the spectra of other galaxies. The fact that a single power-law extinction is slightly preferred when fitting the continuum in some ULIRGS (Tran et al. 2001) could also partially be caused by a GC-like extinction and the mixed model. On the other hand, Thuan et al. (1999) found an extinction curve similar to our results for the extremely metal-poor galaxy SBS 0335-052, also using continuum emission. In the case of the central region of M82, Förster Schreiber et al. (2001) found, using hydrogen lines, that an extinction curve similar to the one in the GC provides a better fit to the data than a single power law. All in all, it is likely that the GC extinction (Lutz et al. 1996), considered to be unusual at the time of discovery, is in general the more widely spread type of extinction.

### 5.7. Broadband Extinction Curve

Since the GC extinction is consistent with many extinction measurements outside of the GC (Sections 5.4 and 5.6), the extinction curve toward the GC (Appendix B) is also useful for other sight lines. We derive from this extinction curve broadband extinction values (Appendix C). In principle, it is necessary to know the extinction amplitude and the intrinsic object spectrum for deriving precise broadband extinctions. The error caused by neglecting these aspects is below 2%. On the other hand, the error due to transmission differences between slightly different, but similarly named, broadband filters can be up to 2.5% (Appendix C). We give in Table 6 broadband extinction ratios relative to the NACO *Ks* band. For extinction

**Table 6**  
Relative Broadband Extinction Values Derived from the GC Extinction Curve

Broadband	$A_{\text{band}}/A_{Ks}$
VIRCAM <i>Y</i>	$4.634 \pm 0.103$
NACO <i>J</i>	$3.051 \pm 0.069$
NACO <i>H</i>	$1.737 \pm 0.027$
NACO <i>Ks</i>	$1.000 \pm 0.000$
NACO <i>L'</i>	$0.450 \pm 0.053$
NACO <i>M'</i>	$0.391 \pm 0.094$
IRAC 1	$0.547 \pm 0.052$
IRAC 2	$0.396 \pm 0.082$
IRAC 3	$0.340 \pm 0.094$
IRAC 4	$0.383 \pm 0.116$

**Notes.** The extinction ratios are obtained from the average of two calculations for the effective filter extinction as described in Appendix C using Vega-like stars with  $A_{\text{Br}\gamma} = 1$  and  $A_{\text{Br}\gamma} = 5$ . The errors are made up of half of the extinction ratio difference between the two different Brackett- $\gamma$  extinction and the extinction curve errors. We assume that the NIR extinction follows a power law of  $\alpha = -2.11 \pm 0.06$ . Broadband filters of other instruments can have another transmission curve. This can result in an additional error of up to 3.5%. For further filters, see Appendix C.

values of many additional filters and for different source spectra, see Appendix C.

### 5.8. Dust Models

Extinction curves, together with the emission spectrum of dust, as well as the elemental abundances and depletions, constrain the properties of interstellar dust. Ideally, the dust model should also be plausible with regard to the formation and destruction of the dust (Compiegne et al. 2011). We use published extinction models which fulfilled most constraints at the time of their publication and compare them with the extinction curve toward the GC.

The classical grain model (Mathis et al. 1977) is composed of silicate and graphite grains, where both follow a power-law size distribution with a lower and an upper cutoff for the exclusion of very large and very small grains. Li & Draine (2001) improved this simple model to size distributions which include even smaller grains in order to account for the polycyclic aromatic hydrocarbon (PAH) emissions by interstellar clouds. We use a slight variant of this dust model considered by Weingartner & Draine (2001) (Wg-model), who also consider different  $R_V$ . This model consists of a trimodal carbonaceous grain size distribution and a simple silicate grain size distribution. With increasing  $R_V$ , the number of small grains decreases while the maximum grain size increases.

Similarly to most later models the Wg-models do not have the H<sub>2</sub>O features at 3  $\mu$ m and 6  $\mu$ m. For constraining the dust properties, independent of the features, we exclude the four lines concerned in our quantitative comparisons. We also exclude the lines beyond 8  $\mu$ m because the silicate feature is not modeled in all works and in no case matches our silicate extinction toward the GC. In addition, by excluding these features we are also more likely to match other extinction measurements in the infrared, such as, for example, Indebetouw et al. (2005) and Nishiyama et al. (2009), where the features could not be measured due to too low spectral resolution. We fit all models to the data by adjusting the extinction curve with a global scaling factor.

**Table 7**  
Goodness of Fit of Different Dust Models

Author	Model	Total $\chi^2/\text{dof}$	Best-fit $\chi^2/\text{Points of NIR}$	Best-fit $\chi^2/\text{Points of MIR}$
Wg01	$R_V = 3.1$	114.3/14	106.6/3/6	7.7/9
Wg01	Case B $R_V = 4.0$	228/14	178/6	51/9
Zu04	BARE-GR-S	18.9/14	4.4/6	14.5/9
Zu04	COMP-AC-S	6.4/12	4.7/4	1.7/9
Dw04		30.9/14	21.7/6	9.2/9
Vo06	$p = 0.18$	111/14	66/6	45/9
Vo06	$p = 0.6$	117/14	111/6	5.2/9

**Notes.** We fit the different dust models to our data by scaling the full extinction curve. The NIR data are between 1 and  $2.8\ \mu\text{m}$ , the MIR lines are between  $3.7$  and  $7.5\ \mu\text{m}$ . In  $\chi^2/\text{points}$  we give the number of data points used for the fitting which are within the NIR and MIR. The models are from Weingartner & Draine (2001), Dwek (2004), Zubko et al. (2004), and Voshchinnikov et al. (2006).

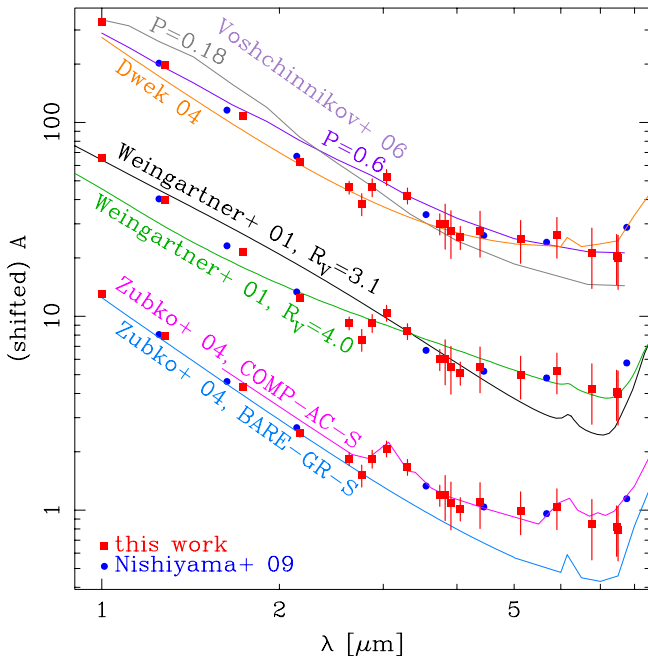


**Figure 9.** Comparison of our data with other data and models. To our extinction measurements derived from hydrogen lines (red boxes), we add the inner bulge observations of Nishiyama et al. (2009; blue circles) scaled to our  $A_{\text{Br}\gamma}$ . The models (lines) are from Weingartner & Draine (2001), Zubko et al. (2004), Dwek (2004), and Voshchinnikov et al. (2006). Everything apart from the lowest data is shifted for better visualization.

(A color version of this figure is available in the online journal.)

All Wg-models have a relatively flat NIR slope  $\alpha \geq -1.7$  and hence fit the data badly in the NIR ( $\lambda < 2.8\ \mu\text{m}$ ), see Table 7. They differ from each other in the MIR. There the models with higher  $R_V$  are flatter. On the one hand, when fitting all lines the models with  $R_V \geq 4.0$  have a worse  $\chi^2$  than the  $R_V = 3.1$  model because of the flatter slope of the  $R_V \geq 4.0$  models in the  $K$  band, which is due to the smaller extinction errors more important than the MIR. On the other hand, the  $R_V = 3.1$  model is incompatible with the data of Nishiyama et al. (2009) in the MIR, see Figure 9. Compared with the Nishiyama et al. (2009) data, the models with  $R_V \geq 4.0$  are a better fit, although none of the Wg-models show such a strong and sharp flattening from NIR to MIR as observed.

One possibility for more complex dust models is the inclusion of voids in the dust grains (Voshchinnikov et al. 2006). In this model, mainly two size distributions of porous silicate grains and one of small graphite grains contribute to the extinction. Still, the extinction features shortward of  $7\ \mu\text{m}$  are unexplained.

This model has the advantage that the NIR slope between  $J$  and  $K$  depends on the porosity. None of their three models with different porosity and also no linear combination of these models can fit our data, see Figure 9 and Table 7.

Zubko et al. (2004) obtained dust models by fitting grain size distribution to an  $R_V = 3.1$  extinction curve, dust emission, and elemental abundances. They use the extinction dispersion between different sight lines as their error estimate. Thus, the extinction has a relatively small weight which could be part of the reason why various dust models can fit their data. Zubko et al. (2004) used different element abundances which have some impact on the result in the case of carbon abundances. We only use their solar abundances. More likely, the real solar abundances (Asplund et al. 2009) are smaller than those used by Zubko et al. (2004). However, the abundances in H II regions are higher than the solar abundances (Asplund et al. 2009) and at least the B-star carbon abundance is too small to cause the observed magnitude of extinction (Li 2005).

The simplest model of Zubko et al. (2004), BARE-GR, consists of only graphite, PAHs, and silicate grains and as such is similar to the Wg-models. BARE-GR only uses graphite grains smaller than  $300\ \text{nm}$  while the Wg-models use grains up to  $0.8\ \mu\text{m}$  and  $5\ \mu\text{m}$ , respectively. Since grain sizes around  $300\ \text{nm}$  cause the steepest infrared slopes in contrast to grains of other sizes (Moore et al. 2005; Gao et al. 2009), the NIR extinction slope of the BARE-GR model is steeper than that of Wg-models. Overall, the BARE-GR model can fit the data with  $\chi^2/\text{dof} = 18.9/14$  relatively well. But this model does not have the  $\text{H}_2\text{O}$  features in contrast to the ISO-SWS spectrum. Because this model nearly does not flatten at all in the MIR, it cannot fit the inner bulge data of Nishiyama et al. (2009), see Figure 9.

The COMP models of Zubko et al. (2004) use, in addition to silicate and carbonaceous grains, composite grains consisting of silicates, organic refractory material, water ice, and voids. These models seem to be more promising for the GC, because they contain water ice which is visible in extinction features toward the GC. The best-fitting subtype is AC in which the carbon is mainly amorphous. The composite particles are, with sizes up to  $0.8\ \mu\text{m}$ , bigger than the other particles. The other subtypes of composite models have a steeper slope, at least in the MIR, and hence make a worse fit to the data. The COMP-AC-S model has a  $\chi^2/\text{dof} = 6.4/12$ , slightly better than the BARE-GR-S model. In contrast to the other models, it also matches the Nishiyama et al. (2009) data, see Figure 9.

Dwek (2004) added metallic needles to the BARE-GR model of Zubko et al. (2004). The extinction caused by the needles rises with wavelength up to  $8\ \mu\text{m}$ , thus flattening the Wg-model between  $3$  and  $8\ \mu\text{m}$ , see Figure 9. The extinction



due to needles drops fast longward of  $8\ \mu\text{m}$  for avoiding a weakening of the silicate feature. This model does not fit the data with  $\chi^2/\text{dof} = 30.9/14$ . The inconsistency is caused by an overly gradual transition to a flatter slope around  $3\ \mu\text{m}$ , while the observed slopes change faster, see Figure 9. While it might be possible to fit our data better with some dust model variant which consists of metallic needles as well as simple carbonaceous and silicate grains, finding a fit to the data will not be easy, since the extinction due to both components varies so slowly with wavelength that it is difficult to obtain the observed sharp flattening around  $3\ \mu\text{m}$ .

All together, the COMP-AC-S model of Zubko et al. (2004) seems to be the best model for extinction toward the GC because of its best  $\chi^2/\text{dof}$  and the presence of the  $\text{H}_2\text{O}$  features. However, the lack of  $\text{H}_2\text{O}$  ice features in most sight lines (Rawlings et al. 2003; Whittet et al. 1997), while MIR flattening is observed in many regions (Zasowski et al. 2009; Jiang et al. 2003, 2006; Gao et al. 2009; Flaherty et al. 2007; Román-Zúñiga et al. 2007; Nishiyama et al. 2009; Indebetouw et al. 2005), renders the idea that composite particles glued by ices are responsible the flat MIR extinction questionable, also for the GC. This is because if composite particles can exist only together with ices, the other regions should show a steeper MIR extinction than the GC. However, because the sight lines with extinction probed in the MIR do not overlap with the sight lines which are tested for  $\text{H}_2\text{O}$  ice, it is still possible that the ice feature could exist in most sight lines with flatter MIR extinction.

An alternative model could be that something else aside from ices produces the flat extinction in the MIR toward the GC and elsewhere, and toward the GC additional pure ice grains produce the extinction features. However, all other models tested here have the problem that they do not have at once a steep NIR extinction and a flat MIR extinction. It is perhaps possible to change the shape of the extinction curves within the models without changing the type of particles in the model. However, this seems difficult for the pure carbonaceous and silicate grain model, because a smooth particle size distribution of carbonaceous and silicate grains should also produce a smooth extinction curve. It might be possible, on the other hand, to change the extinction shape only around  $3\ \mu\text{m}$  by omitting only  $\text{H}_2\text{O}$  ice from the composite particles in the COMP-AC-S model. If this does not change the other extinction properties of the dust such a model could fit the extinction also in other sight lines.

For solving the issue, further modeling seems to be necessary, maybe concentrating first on the detailed extinction curve toward the GC. In the future, similarly detailed extinction curves in other sight lines would also be very useful. Especially promising could be searching for the  $\text{H}_2\text{O}$  ice feature in sight lines which are already probed by broadband measurements. Also, adding more extinction measurements in between for testing the commonness of the sharp transition to a flatter extinction in the MIR might be very interesting for further study.

## 6. SUMMARY

The simplest way to derive an extinction curve is to observe a well-understood object at different wavelengths, including at least one extinction-free wavelength. The minispiral in the GC fulfills these conditions. It is an H II region and Case B is valid. As extinction-free emission we use the 2 cm radio continuum observed with the VLA. In the infrared, we obtain line fluxes between  $1.28\ \mu\text{m}$  and  $2.17\ \mu\text{m}$  from SINFONI. For lines at longer wavelengths of up to  $19\ \mu\text{m}$  we use ISO-SWS observations. We obtain the following results.

1. By interpolation we obtain  $A_{2.166\ \mu\text{m}} = 2.62 \pm 0.11$  as the average  $2.166\ \mu\text{m}$  extinction of the ISO field of  $14'' \times 20''$  about Sgr A\*.
2. Using the extinction map of Schödel et al. (2010) for the relative spatial extinction we obtain, for the direction toward Sgr A\*:  $A_H = 4.21 \pm 0.10$ ,  $A_{K_S} = 2.42 \pm 0.10$ , and  $A_{L'} = 1.09 \pm 0.13$ .
3. Schödel et al. (2010) measured the total luminosity modulus of the red clump consisting of the extinction and distance modulus toward the GC. Since we measure the extinction independent of the distance, the combination of Schödel et al. (2010) with our extinction yields the distance  $R_0$ , the distance to the GC: we obtain  $R_0 = 7.94 \pm 0.65\ \text{kpc}$  in agreement with current measurements.
4. The extinction in the NIR ( $1.2\text{--}2.8\ \mu\text{m}$ ) is well fitted by a power law of slope  $\alpha = -2.11 \pm 0.06$ . This law is steeper than the value of about  $\alpha \approx -1.75$ , which was mostly reported in the literature before 2004, see, for example Draine (1989). However, since 2005 most publications about diffuse extinction toward the bulge and Galactic disk (for example, Stead & Hoare 2009) yield a steeper law. We obtain  $\alpha = -2.07 \pm 0.16$  as a weighted average of all publications about diffuse extinction since 2005.
5. At longer wavelengths, several extinction features are visible, such as  $\text{H}_2\text{O}$  at  $3.1\ \mu\text{m}$  and silicates at  $9.7\ \mu\text{m}$ . Even aside from such features, the extinction is higher than expected from extrapolating the NIR power law. Our data agree well with several IRAC publications for the inner bulge, such as Nishiyama et al. (2009), for example. Because we are able to use many lines, it is apparent that the change in slope is sharper and stronger than in any of the extinction curves produced by pure carbonaceous and silicate grains (Weingartner & Draine 2001). The best-fitting model adds composite particles which contain also  $\text{H}_2\text{O}$  ice (Zubko et al. 2004).

## APPENDIX A

### CORRECTING FOR THE EXTINCTION LAW FLATTENING BIAS DUE TO INHOMOGENEOUS EXTINCTION

Here, we estimate the extinction law flattening bias due to inhomogeneous extinction.

We make the assumption that the true extinction map  $A_i(\lambda)$ , for resolution element  $i$  and wavelength  $\lambda$ , has the same relative spatial distribution of extinction as the Schödel et al. (2010) map, such that we can obtain the extinction map at a given wavelength  $\lambda$  via a simple scaling of an (as yet unknown) factor  $x(\lambda)$ :

$$A_i(\lambda) = x(\lambda) \times A_{i\text{Sch}}. \quad (\text{A1})$$

We then derive an unextincted Brackett- $\gamma$  flux map from our observed Brackett- $\gamma$  flux map, using the extinction map of Schödel et al. (2010; scaled to our measured Brackett- $\gamma$  extinction) as model for the spatial inhomogeneity in the extinction at this wavelength. For resolution element  $i$ , the unextincted flux map can be written as

$$F_i(\lambda = \text{Br } \gamma)_{\text{unext}} = F_i(\lambda = \text{Br } \gamma)_{\text{obs}} \times 10^{0.4 x_0 A(\text{map})_{\text{Sch}}}. \quad (\text{A2})$$

Here, we use as scaling factor,  $x_0$ , our integrated measurement of the Brackett- $\gamma$  extinction (Section 4.2), divided by the

(observed) flux-weighted extinction of the Schödel et al. (2010) map:

$$x_0 = A(\lambda = \text{Br } \gamma)_{\text{integrated, measured}} \times \left( \frac{\sum_{i \in \text{ISO}} F_i(\lambda = \text{Br } \gamma)_{\text{ext}} A_{i \text{ Sch}}}{\sum_{i \in \text{ISO}} F_i(\lambda = \text{Br } \gamma)_{\text{ext}}} \right)^{-1}. \quad (\text{A3})$$

We use the unextinguished Brackett- $\gamma$  flux map as a model for the spatial distribution of the intrinsic (unextinguished) flux at all wavelengths (i.e., the correct distribution of relative flux weights).

The true (extinction-law-conserving) integrated extinction should be flux-weighted by the unextinguished flux, not the observed flux:

$$A(\lambda)_{\text{integrated, true}} = x(\lambda) \times \frac{\sum_{i \in \text{ISO}} F_i(\lambda = \text{Br } \gamma)_{\text{unext}} A_{i \text{ Sch}}}{\sum_{i \in \text{ISO}} F_i(\lambda = \text{Br } \gamma)_{\text{unext}}}. \quad (\text{A4})$$

Our extinction measurement, on the other hand, measures rather the ratio of integrated fluxes:

$$A(\lambda)_{\text{integrated, measured}} = -2.5 \log \left( \frac{\sum_{i \in \text{ISO}} F_i(\lambda = \text{Br } \gamma)_{\text{ext}}}{\sum_{i \in \text{ISO}} F_i(\lambda = \text{Br } \gamma)_{\text{unext}}} \right). \quad (\text{A5})$$

In this equation, areas with smaller extinction have higher observed fluxes relative to the unextinguished flux and thus are given a higher weight. Upon integration this then leads to a smaller measured extinction than the true integrated extinction of Equation (A4).

To estimate this bias, we simulate our extinction measurements, weighting the intrinsic extinction,  $x(\lambda)A_{i \text{ Sch}}$ , by the unextinguished flux weights derived from the Brackett- $\gamma$  map:

$$A(\lambda)_{\text{integrated, simulated}} = -2.5 \times \log \left( \frac{\sum_{i \in \text{ISO}} 10^{-0.4x(\lambda)A_{i \text{ Sch}}} F_i(\lambda = \text{Br } \gamma)_{\text{unext}}}{\sum_{i \in \text{ISO}} F_i(\lambda = \text{Br } \gamma)_{\text{unext}}} \right). \quad (\text{A6})$$

For every SINFONI line at wavelength  $\lambda$  we find an  $x(\lambda)$  which, when substituted in Equation (A6), results in our measured extinction  $A(\lambda)_{\text{integrated, measured}}$ . The calculation is carried out over the same area (ISO) used in the extinction measurement for each line. The bias at a given wavelength  $\lambda$  is then

$$\Delta A(\lambda) = A(\lambda)_{\text{integrated, true}} - A(\lambda)_{\text{integrated, simulated}}. \quad (\text{A7})$$

This correction must be applied to  $A(\lambda)_{\text{integrated, measured}}$  in order to obtain the correct (extinction-law-conserving) extinction. The biggest correction occurs for the highest extinction (Paschen- $\beta$ ). Even for this line the correction is only 0.08 mag, smaller than the extinction error of 0.11 mag.

## APPENDIX B

### INTERPOLATING THE EXTINCTION CURVE

We use the continuum of the ISO-SWS spectrum in order to constrain the shape of the extinction curve in the MIR. The unextinguished continuum cannot be modeled with a single simple model such as a single blackbody or gray body. Instead, we correct the measured continuum close to the hydrogen lines by using the extinction of the lines. We then interpolate the resulting points using simple models for sections of the spectrum, described in

**Table 8**  
Interpolated Infrared Extinction Curve

$\lambda(\mu\text{m})$	$A(\text{GC})$	$\delta A(\text{GC})$
1.00009	13.1075	0.3
1.00984	12.8529	0.2925
1.0197	12.6033	0.285
1.02964	12.3586	0.2776
1.03969	12.1186	0.2701
1.04983	11.8832	0.2626
1.06007	11.6525	0.2551
1.07041	11.4262	0.2477
1.08086	11.2043	0.2402
1.0914	10.9867	0.2327

**Notes.** Our extinction curve. The second column is the average extinction toward the central  $14'' \times 20''$  of the GC. The errors include all effects. Some effects matter only for comparison over big wavelength ranges. Locally, the error is smaller for most of the ISO-SWS range (2.6–27  $\mu\text{m}$ ). This curve can be used for  $A(\lambda)$  in formula (C1) for obtaining the extinction for other objects and filters. Scaled to other absolute extinctions it can also be useful outside the Galactic center.

(This table is available in its entirety in a machine-readable form in the online journal. A portion is shown here for guidance regarding its form and content.)

the paragraph below. After this, we obtain the extinction curve by dividing the interpolated extinction-corrected continuum by the observed continuum. By applying this method, we use the extinction of the hydrogen lines to obtain extinction values in regions where no hydrogen lines are available.

Between 2.62 and 7.6  $\mu\text{m}$ , we fit the extinction-corrected continuum points with a second-order polynomial in log-log space. At longer wavelengths however the interpolation is less certain, due to the fact that there are fewer lines, larger extinction errors, and silicate emission in the GC region (Kemper et al. 2004). For the continuum up to 12  $\mu\text{m}$  we use the GC continuum of Kemper et al. (2004), which contains silicate emission, scaled such that it fits our two data points in this wavelength range. A 240 K blackbody is a good approximation to the extinguished continuum between 12 and 15  $\mu\text{m}$ . In this range there are no significant extinction features. We extrapolate this blackbody up to 26  $\mu\text{m}$ , scaling it such that the unextinguished continuum close to both lines in this range is fit by the blackbody, and use it as a model for the continuum between 12 and 26  $\mu\text{m}$ . We combine the three different continua with smooth transitions around 7  $\mu\text{m}$  and 12  $\mu\text{m}$ , see Figure 10.

In a similar way, we make a smooth transition to the  $\alpha = -2.11$  power law shortward of 2.75  $\mu\text{m}$ . We continue the interpolation by a  $\alpha = -2.02$  power law shortward of 1.28  $\mu\text{m}$ . We also correct unphysical jumps in the extinction curve, such as the one at 4.07  $\mu\text{m}$ , due to calibration errors of the ISO-SWS data. For this we adjust the extinction curve locally with linear interpolation. We interpolate the extinction curve we obtain, excluding spectral lines, with splines (Table 8). The spectral resolution of this interpolation is not high enough to fully resolve all features, such as, e.g., the CO feature at 4.7  $\mu\text{m}$ .

## APPENDIX C

### EFFECTIVE BROADBAND FILTER EXTINCTIONS

A complication in correcting for extinction in broadband flux measurements is that the extinction that should be associated

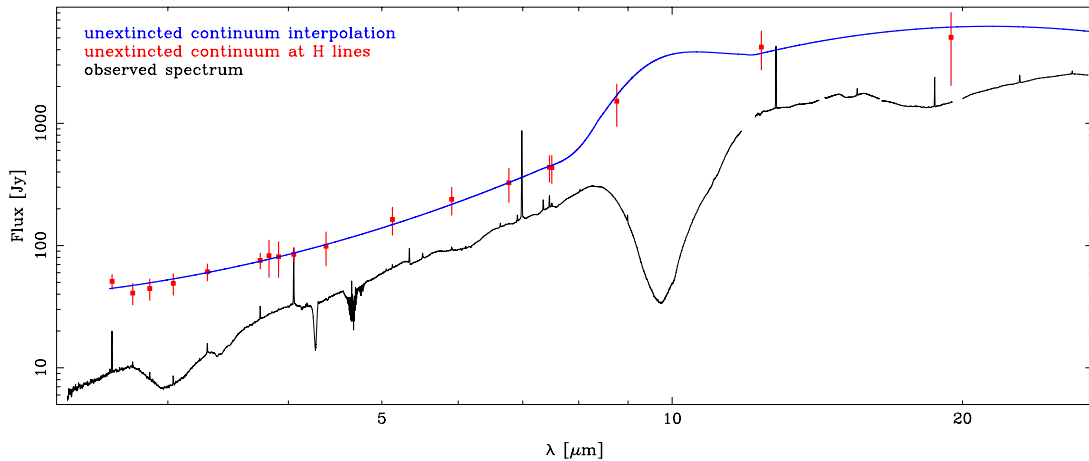


**Figure 10.** Measured and unextincted MIR continuum toward the GC. The black line is the observed ISO-SWS spectrum. We unextinct the continuum around the hydrogen lines by the hydrogen line extinctions there (red boxes). We interpolate these points to obtain the unextincted continuum (blue line).

(A color version of this figure is available in the online journal.)

with a given filter varies with both the intrinsic spectrum of the source and the strength of the extinction.

Since we use spectral lines in this paper to constrain the extinction law, the wavelengths to associate with the extinction measurements are well defined. Also the interpolated extinction (Appendix B) has well-defined wavelengths. Thus, we can explicitly calculate the extinction values for a given broadband filter, like Espinoza et al. (2009), using the equation

$$A_{\text{filter}} = -2.5 \times \log \left( \frac{\int \lambda F_{\lambda}(\lambda) S(\lambda) R(\lambda) d\lambda}{\int \lambda F_{\lambda}(\lambda) S(\lambda) d\lambda} \right). \quad (\text{C1})$$

Here,  $F_{\lambda}(\lambda)$  is the intrinsic flux density of the source, which when multiplied with the wavelength,  $\lambda$ , is proportional to the number distribution of photons with wavelength.  $S(\lambda)$  is the wavelength-dependent throughput of telescope, instrument, and atmosphere. We also define here  $R(\lambda) = 10^{-0.4 A(\lambda)}$  as a “reddening factor” to separate the extinction from the intrinsic flux.

We use our interpolated extinction curve for  $A(\lambda)$  (see Appendix B and Table 8) in formula (C1) to calculate the effective broadband filter extinction values for a range of commonly used infrared filters. The results are presented in Table 9. As source spectrum we use primarily a blackbody of 9480 K. For stars of this temperature, there is no major difference between the real spectrum and the correct blackbody in the infrared. The use of such a star also has the advantage that a similar star is used for the definition of the Vega magnitude system. In addition, we also compute the effective filter extinctions for a bright Sgr A\* like spectrum (Eisenhauer et al. 2005; Gillessen et al. 2006) which follows a power law with a slope  $\beta = 0.5$  in  $\nu L_{\nu}$  (Hornstein et al. 2007; Dodds-Eden et al. 2009) as an example of a very red source. For  $S(\lambda)$  we use the atmospheric transmission multiplied with the instrument transmission. For all Paranal filters we use the atran transmission models (Lord 1992) from Cerro Panchon for the atmosphere, with airmass 1 and 2.3 mm water vapor column from the Gemini Web site.<sup>7</sup> For the VISIR filters we use the filter transmissions from the instrument Web site.<sup>8</sup> We obtain the VIRCAM filters from the instrument Web site.<sup>9</sup> For the NIRC2

filters, which we obtain from the instrument Web site,<sup>10</sup> we use a Mauna Kea atmosphere of airmass 1.5 and 1.6 mm water vapor column from the Gemini Web site.<sup>7</sup> For these instruments, only in the case of VIRCAM are the wavelength-dependent quantum efficiency (QE) and mirror reflectivity available. We use them for our calculation. However, including QE and mirror reflectivity changes the extinction only by less than 0.07% relatively. For the other instruments we assume that the throughput of the instrument is apart from the filter not wavelength dependent within a filter. For 2MASS we use the full transmissions including the atmosphere from the project Web site.<sup>11</sup> We obtain the NICMOS transmissions from the instrument Web site<sup>12</sup> as in the case of the IRAC transmissions.<sup>13</sup>

Although, strictly speaking, it is necessary to calculate the effective broadband extinction on a per spectrum basis, the differences in the effective extinction for different source SEDs are mostly relatively small, even for the high extinction of the GC. For example, the difference in effective extinction between a blue spectrum (Vega) and a red spectrum (Sgr A) is only 0.056 mag in the  $H$  band and 0.026 mag in the  $K_s$  band.

We test the influence of different magnitudes of extinctions on broadband extinctions. The  $H$ -band extinction derived from  $A_{\text{Br}\gamma} = 2.62$  is 4.65 mag, while the  $H$ -band extinction derived from  $A_{\text{Br}\gamma} = 0.5$  is 0.91 mag. Assuming linear scaling of the  $H$ -band extinction with the Brackett- $\gamma$  extinction the expected  $H$ -band extinction (scaled up from  $A_{\text{Br}\gamma} = 0.5$ ) is  $0.91 \text{ mag} \times 2.62/0.5 = 4.77 \text{ mag}$ . Thus, the deviation from linearity (the nonlinearity) is 0.12 mag in this case. In the  $K_s$  band the nonlinearity is, with 0.029 mag, much smaller for the same value of  $A_{\text{Br}\gamma}$ . We find that the nonlinearity is of the order of the measurement error for  $A_{\text{band}} \leq 4$ .

For most objects, for which the extinction is not significantly higher than in the GC, it is sufficient to use the extinction closest to the measured extinction in Table 9 renormalized to the correct absolute extinction. For very high extinctions or different filters it is necessary to calculate the filter extinctions from formula (C1) using the interpolated extinction curve given in Table 8.

<sup>7</sup> <http://www.gemini.edu/?q=node/10789>

<sup>8</sup> <http://www.eso.org/sci/facilities/paranal/instruments/visir/inst/index.html>

<sup>9</sup> <http://www.eso.org/sci/facilities/paranal/instruments/vircam/inst/>

<sup>10</sup> <http://www2.keck.hawaii.edu/inst/nirc2/filters.html>

<sup>11</sup> [http://www.ipac.caltech.edu/2mass/releases/second/doc/sec3\\_1b1.html#s16](http://www.ipac.caltech.edu/2mass/releases/second/doc/sec3_1b1.html#s16)

<sup>12</sup> <http://www.stsci.edu/hst/nicmos/design/filters>

<sup>13</sup> <http://ssc.spitzer.caltech.edu/irac/calibrationfiles/spectralresponse>



**Table 9**  
Extinction of Broadband Filters for Different Brackett- $\gamma$  Extinctions

Instrument	Filter	$A(A_{\text{Br}\gamma} = 2.62)$ 9480 K	$A(A_{\text{Br}\gamma} = 0.5)$ 9480 K	$A(A_{\text{Br}\gamma} = 6)$ 9480 K	$A(A_{\text{Br}\gamma} = 2.40)$ $\beta = 0.5$
NACO	<i>J</i>	$8.16 \pm 0.12$	$1.62 \pm 0.03$	$17.90 \pm 0.26$	$7.42 \pm 0.11$
NACO	<i>H</i>	$4.65 \pm 0.11$	$0.91 \pm 0.02$	$10.29 \pm 0.25$	$4.21 \pm 0.10$
NACO	<i>Ks</i>	$2.67 \pm 0.11$	$0.52 \pm 0.02$	$6.02 \pm 0.26$	$2.42 \pm 0.10$
NACO	<i>L'</i>	$1.20 \pm 0.14$	$0.23 \pm 0.03$	$2.73 \pm 0.32$	$1.09 \pm 0.13$
NACO	<i>M'</i>	$1.05 \pm 0.25$	$0.20 \pm 0.05$	$2.37 \pm 0.57$	$0.95 \pm 0.23$
VISIR	PAH1 (8.6 $\mu\text{m}$ )	$1.73 \pm 0.54$	$0.34 \pm 0.10$	$3.83 \pm 1.23$	$1.60 \pm 0.50$
VISIR	PAH2_2 (11.88 $\mu\text{m}$ )	$1.61 \pm 0.36$	$0.31 \pm 0.07$	$3.66 \pm 0.83$	$1.47 \pm 0.33$
NICMOS	110M	$10.42 \pm 0.19$	$2.07 \pm 0.04$	$22.86 \pm 0.40$	$9.49 \pm 0.18$
NICMOS	145M	$6.00 \pm 0.11$	$1.16 \pm 0.02$	$13.44 \pm 0.25$	$5.47 \pm 0.10$
NICMOS	160W	$4.89 \pm 0.11$	$0.97 \pm 0.02$	$10.61 \pm 0.25$	$4.40 \pm 0.10$
NICMOS	170M	$4.33 \pm 0.11$	$0.83 \pm 0.02$	$9.80 \pm 0.25$	$3.95 \pm 0.10$
NICMOS	222M	$2.50 \pm 0.11$	$0.48 \pm 0.02$	$5.70 \pm 0.26$	$2.28 \pm 0.10$
IRAC	Band 1	$1.47 \pm 0.14$	$0.28 \pm 0.03$	$3.27 \pm 0.32$	$1.31 \pm 0.13$
IRAC	Band 2	$1.06 \pm 0.22$	$0.20 \pm 0.04$	$2.40 \pm 0.50$	$0.97 \pm 0.20$
IRAC	Band 3	$0.91 \pm 0.25$	$0.17 \pm 0.05$	$2.08 \pm 0.57$	$0.83 \pm 0.23$
IRAC	Band 4	$1.02 \pm 0.31$	$0.21 \pm 0.06$	$2.19 \pm 0.67$	$1.01 \pm 0.30$
NIRC2	<i>H</i>	$4.75 \pm 0.11$	$0.93 \pm 0.02$	$10.56 \pm 0.25$	$4.31 \pm 0.10$
NIRC2	<i>K'</i>	$2.73 \pm 0.11$	$0.53 \pm 0.02$	$6.15 \pm 0.26$	$2.48 \pm 0.10$
NIRC2	<i>L'</i>	$1.24 \pm 0.14$	$0.24 \pm 0.03$	$2.80 \pm 0.32$	$1.12 \pm 0.13$
NIRC2	<i>Ms</i>	$1.17 \pm 0.25$	$0.23 \pm 0.05$	$2.66 \pm 0.57$	$1.07 \pm 0.23$
VIRCAM	<i>Y</i>	$12.40 \pm 0.27$	$2.40 \pm 0.05$	$27.77 \pm 0.58$	$11.33 \pm 0.25$
VIRCAM	<i>J</i>	$8.21 \pm 0.12$	$1.60 \pm 0.03$	$18.30 \pm 0.26$	$7.48 \pm 0.11$
VIRCAM	<i>H</i>	$4.68 \pm 0.11$	$0.91 \pm 0.02$	$10.41 \pm 0.25$	$4.24 \pm 0.10$
VIRCAM	<i>Ks</i>	$2.67 \pm 0.11$	$0.51 \pm 0.02$	$6.04 \pm 0.26$	$2.42 \pm 0.10$
2MASS	<i>J</i>	$8.26 \pm 0.12$	$1.64 \pm 0.03$	$18.14 \pm 0.26$	$7.51 \pm 0.11$
2MASS	<i>H</i>	$4.65 \pm 0.11$	$0.90 \pm 0.02$	$10.37 \pm 0.25$	$4.22 \pm 0.10$
2MASS	<i>Ks</i>	$2.58 \pm 0.11$	$0.50 \pm 0.02$	$5.84 \pm 0.26$	$2.34 \pm 0.10$

**Notes.** We calculate filter extinctions for different Brackett- $\gamma$  (2.166  $\mu\text{m}$ ) extinctions. We use blackbodies and power-law source spectra. The error is the uncertainty due to the extinction error. The first column is the average extinction of stars in the central  $14'' \times 20''$  of the GC. The last column is the extinction toward the power-law source Sgr A\* (i.e., using stars in the central  $r \leq 0.5$  of the GC for scaling of  $A_{\text{Br}\gamma}$ ).

## APPENDIX D

### COMPARISON WITH OTHER METHODS FOR THE DETERMINATION OF THE NIR EXTINCTION SLOPE

We derive the NIR extinction slope  $\alpha$  from absolute extinction values at known wavelength. Another way commonly used to compute the near-infrared extinction slope  $\alpha$  is to use stellar colors, using an assumed wavelength to associate with the broadband filters (we hereafter call this the effective wavelength method). For example, the following equation is commonly used to compute the extinction slope  $\alpha$  from *JHK*(s) colors (Stead & Hoare 2009):

$$\frac{E_{J-H}}{E_{H-Ks}} = \frac{\left(\frac{\lambda_J}{\lambda_H}\right)^\alpha - 1}{1 - \left(\frac{\lambda_{Ks}}{\lambda_H}\right)^\alpha}, \quad (\text{D1})$$

where  $\lambda_J$  is some assumed wavelength of the *J* filter, and so on for the other filters. Obviously, it is necessary to know the wavelength that can correctly be associated with the filters for the given source and extinction in order to derive  $\alpha$ . One possibility would be to use the isophotal wavelength ( $\lambda_{\text{iso}}$ ) (Tokunaga & Vacca 2005):

$$F_\lambda(\lambda_{\text{iso}}) = \frac{\int F_\lambda(\lambda) S(\lambda) d\lambda}{\int S(\lambda) d\lambda}. \quad (\text{D2})$$

This means that  $\lambda_{\text{iso}}$  is the wavelength at which the monochromatic flux  $F_\lambda(\lambda_{\text{iso}})$  equals the mean flux in the passband.

More commonly used for extinction purposes is the effective wavelength (Tokunaga & Vacca 2005):

$$\lambda'_{\text{eff unext}} = \frac{\int \lambda^2 F_\lambda(\lambda) S(\lambda) d\lambda}{\int \lambda F_\lambda(\lambda) S(\lambda) d\lambda}. \quad (\text{D3})$$

The effective wavelength defined in this way is the average wavelength of received photons, weighted by the number distribution of received photons at the detector, appropriate for photon counting detectors. This formula is used in two variants: for the calculation of  $\lambda'_{\text{eff unext}}$  the source spectra are not extinguished.

For the calculation of the other variant ( $\lambda'_{\text{eff ext}}$ ), the source spectra are extinguished (Stead & Hoare 2009; Schödel et al. 2010):

$$\lambda'_{\text{eff ext}} = \frac{\int \lambda^2 F_\lambda(\lambda) S(\lambda) R(\lambda) d\lambda}{\int \lambda F_\lambda(\lambda) S(\lambda) R(\lambda) d\lambda}. \quad (\text{D4})$$

We test the accuracy of the methods concentrating on the two definitions of the effective wavelength. To do this we compare the explicitly calculated filter extinctions to those obtained with the effective wavelength method for an extinguished, 9480 K Vega-like blackbody. As test filters we use the NACO *JHKs* filters plus atmosphere and our  $\alpha = -2.11$  extinction law. Using formula (C1), we obtain slightly higher extinctions for the explicit calculation than obtained by applying the extinguished effective wavelength method (formula (D1)), with differences of  $A_{Ks \text{ true}} - A_{Ks \lambda' \text{ eff ext}} = 0.05$  for  $A_{\text{Br}\gamma} = 2.5$

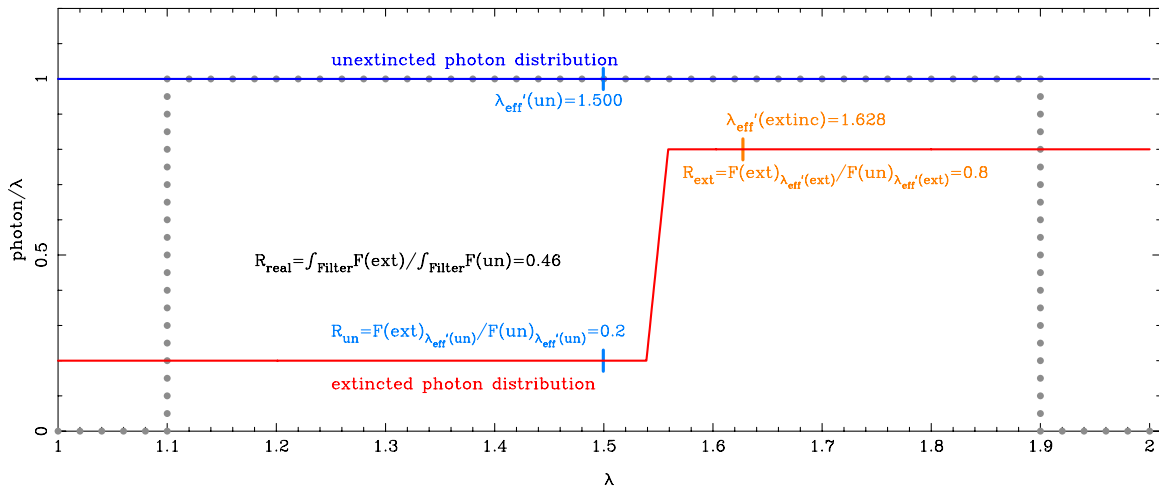


**Figure 11.** Difference between the extinction at (extincted and unextincted) effective wavelengths, and the filter-integrated extinction. A source (blue line, showing unextincted flux) is observed with a broad filter (gray dots). Via an (unrealistic) extinction, the source is extinguished to the red line. In this example, the effective wavelength of the unextincted flux is in the part with high extinction, and the effective wavelength of the extincted flux is in the part with low extinction. The true reddening factor, however, is determined by the integrals over the filter range and has a value between the reddening factors at the two effective wavelengths. For more realistic extinction curves this effect is much smaller, but not always negligible.

(A color version of this figure is available in the online journal.)

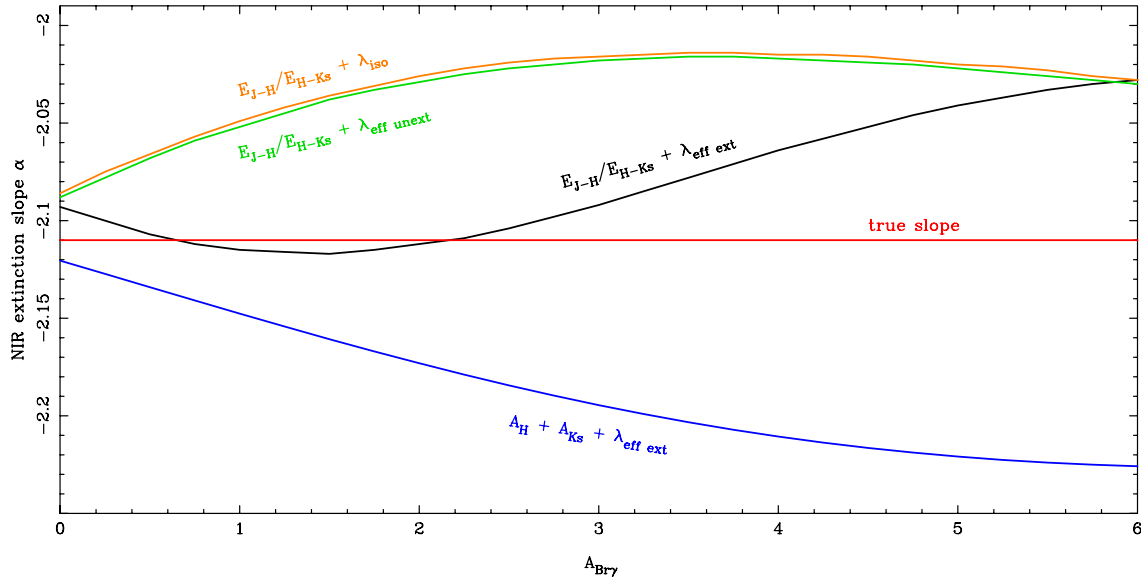


**Figure 12.** Comparison of the true near-infrared extinction slope  $\alpha$  with the  $\alpha$  obtained using common methods. We use the NACO *JHKs* filters with atmosphere and a 9480 K blackbody, simulating common measurements. For obtaining  $\alpha$  from  $E_{J-H}/E_{H-Ks}$  we use formula (D1). The results are displayed as follows: orange, the use of the isophotal wavelength in formula (D1); green, the use of the effective wavelength of the unextincted flux in formula (D1); black, the use of the effective wavelength of the extincted flux in formula (D1); and blue, the computation of  $\alpha$  from absolute  $A_H$  and  $A_{Ks}$ , using the extincted effective wavelengths. The true slope is shown as the red line.

(A color version of this figure is available in the online journal.)

(for lower extinction the difference is much less,  $A_{Ks \text{ true}} - A_{Ks \lambda' \text{ eff ext}} = 0.013$  for  $A_{Bry} = 1$ ). Similarly, we obtain  $A_{Ks \text{ true}} - A_{Ks \lambda' \text{ eff unext}} = -0.012$  for  $A_{Bry} = 2.5$  when we use the unextincted effective wavelengths.

The reason for these discrepancies is illustrated via an exaggerated example in Figure 11. To obtain the correct value of the true extinction, it is necessary to consider the photon distribution, integrated over the filter, of both the unextincted and the extincted source. Yet the two effective wavelength methods each consider only one of the above photon distributions. In the case of the unextincted source: because a larger proportion of the photons is transmitted through the extinction at longer wavelength than at  $\lambda'_{\text{eff unext}}$ , the true filter extinction is smaller than at  $\lambda'_{\text{eff unext}}$ . The opposite is true at  $\lambda'_{\text{eff ext}}$ .

In summary both “effective” wavelengths deviate from the true extinction, because these effective wavelengths are not the effective extinction wavelengths. As a result it is not correct to use these “effective” wavelengths to calculate the extinction appropriate for broadband filters from our extinction curve. The true wavelength for extinction measurements  $\lambda_{\text{true}}$  is the wavelength at which the extincted object is extinguished by the same amount of extinction as in the explicit calculation of formula (C1).  $\lambda_{\text{true}}$  depends on the optical system, object SED, strength of extinction, and the shape of the extinction law. However, since Stead & Hoare (2009) and Schödel et al. (2010), e.g., measured the broadband extinctions directly their extinctions are correct at least for the specific source, filter, and extinction strength combinations used in the determination.

More important is the issue of effective wavelengths for the determination of  $\alpha$  from measured broadband extinctions. To test this we calculate  $\alpha$ , using either  $\lambda_{\text{iso}}$ ,  $\lambda'_{\text{eff unext}}$ , or  $\lambda'_{\text{eff ext}}$  in formula (D1) (method of relative extinction). We also calculate  $\alpha$  from the absolute  $A_H$  and  $A_{K_s}$  using  $\lambda'_{\text{eff ext}}$ , as is done in Schödel et al. (2010). We then compare the obtained values of  $\alpha$  with the input  $\alpha = -2.11$ , see Figure 12.

Since none of the methods obtain the true extinction values, it is not surprising that none of the methods obtain the true extinction slope  $\alpha$ . The best method for obtaining  $\alpha$  is using  $\lambda'_{\text{eff ext}}$  and formula (D1): for extinctions  $A_{\text{Br}\gamma} \leq 4$  there is less than 0.046 deviation of  $\alpha$  from the input  $\alpha = -2.11$ . The other methods can result in larger deviations of up to 0.11 for the same range of extinction.

The difference between the  $\alpha$  obtained using  $\lambda'_{\text{iso}}$  and  $\lambda'_{\text{eff unext}}$  is only  $\Delta\alpha \approx 0.01$ . In contrast Stead & Hoare (2009) obtain a difference of around  $\Delta\alpha = 0.2$ . The reason for this could be the slightly different photometric system, but perhaps more likely, the difference between a 9480 K blackbody and a K2III spectrum. Given this big difference in  $\Delta\alpha$ , it is unclear if using  $\lambda'_{\text{eff unext}}$  is also the best approximation to the true  $\alpha$  for instruments and source spectra other than those tested here.

## REFERENCES

- Abuter, R., Schreiber, J., Eisenhauer, F., Ott, T., Horrobin, M., & Gillesen, S. 2006, *New Astron. Rev.*, **50**, 398
- Asplund, M., Grevesse, N., Sauval, A. J., & Scott, P. 2009, *ARA&A*, **47**, 481
- Baker, J. G., & Menzel, D. H. 1938, *ApJ*, **88**, 52
- Bartko, H., et al. 2009, *ApJ*, **697**, 1741
- Bartko, H., et al. 2010, *ApJ*, **708**, 834
- Becklin, E. E., Gatley, I., & Werner, M. W. 1982, *ApJ*, **258**, 135
- Becklin, E. E., & Neugebauer, G. 1968, *ApJ*, **151**, 145
- Beintema, D. A., Salama, A., & Lorente, R. 2003, in *The Calibration Legacy of the ISO Mission*, ed. L. Metcalfe, A. Salama, S. B. Peschke, & M. F. Kessler (ESA Special Publication, Vol. 481; Noordwijk: ESA), **215**
- Blum, R. D., Ramirez, S. V., Sellgren, K., & Olsen, K. 2003, *ApJ*, **597**, 323
- Blum, R. D., Sellgren, K., & Depoy, D. L. 1996, *ApJ*, **470**, 864
- Bohlin, R. C., Savage, B. D., & Drake, J. F. 1978, *ApJ*, **224**, 132
- Bonnet, H., et al. 2003, *Proc. SPIE*, **4839**, 329
- Brown, R. L., & Liszt, H. S. 1984, *ARA&A*, **22**, 223
- Butchart, I., McFadzean, A. D., Whittet, D. C. B., Geballe, T. R., & Greenberg, J. M. 1986, *A&A*, **154**, L5
- Calzetti, D. 2001, *PASP*, **113**, 1449
- Calzetti, D., Armus, L., Bohlin, R. C., Kinney, A. L., Koornneef, J., & Storchi-Bergmann, T. 2000, *ApJ*, **533**, 682
- Cardelli, J. A., Clayton, G. C., & Mathis, J. S. 1989, *ApJ*, **345**, 245
- Chiar, J. E., Tielens, A. G. G. M., Whittet, D. C. B., Schutte, W. A., Boogert, A. C. A., Lutz, D., van Dishoeck, E. F., & Bernstein, M. P. 2000, *ApJ*, **537**, 749
- Compiègne, M., et al. 2011, *A&A*, **525**, A103
- Cunha, K., Sellgren, K., Smith, V. V., Ramirez, S. V., Blum, R. D., & Terndrup, D. M. 2007, *ApJ*, **669**, 1011
- Dambis, A. K. 2009, *MNRAS*, **396**, 553
- de Graauw, T., et al. 1996a, *A&A*, **315**, L49
- de Graauw, T., et al. 1996b, *A&A*, **315**, L345
- Dodds-Eden, K., et al. 2009, *ApJ*, **698**, 676
- Draine, B. T. 1989, in *Infrared Spectroscopy in Astronomy*, ed. E. Böhm-Vitense (ESA Special Publication, Vol. 290; Noordwijk: ESA), **93**
- Draine, B. T. 2003, *ARA&A*, **41**, 241
- Dwek, E. 2004, *ApJ*, **611**, L109
- Eisenhauer, F., Schödel, R., Genzel, R., Ott, T., Tecza, M., Abuter, R., Eckart, A., & Alexander, T. 2003a, *ApJ*, **597**, L121
- Eisenhauer, F., et al. 2003b, *Proc. SPIE*, **4841**, 1548
- Eisenhauer, F., et al. 2005, *ApJ*, **628**, 246
- Espinoza, P., Selman, F. J., & Melnick, J. 2009, *A&A*, **501**, 563
- Fitzpatrick, E. L. 2004, in *ASP Conf. Ser. 309, Astrophysics of Dust*, ed. A. N. Witt, G. C. Clayton, & B. T. Draine (San Francisco, CA: ASP), **33**
- Fitzpatrick, E. L., & Massa, D. 2009, *ApJ*, **699**, 1209
- Flaherty, K. M., Pipher, J. L., Megeath, S. T., Winston, E. M., Gutermuth, R. A., Muzerolle, J., Allen, L. E., & Fazio, G. G. 2007, *ApJ*, **663**, 1069
- Förster Schreiber, N. M., Genzel, R., Lutz, D., Kunze, D., & Sternberg, A. 2001, *ApJ*, **552**, 544
- Fritz, T. K., et al. 2010, *ApJ*, **721**, 395
- Froebrich, D., & del Burgo, C. 2006, *MNRAS*, **369**, 1901
- Gao, J., Jiang, B. W., & Li, A. 2009, *ApJ*, **707**, 89
- Gao, J., Jiang, B. W., & Li, A. 2010, *Earth Planets Space*, **62**, 63
- Genzel, R., Eisenhauer, F., & Gillesen, S. 2010, *Rev. Mod. Phys.*, **82**, 3121
- Genzel, R., Pichon, C., Eckart, A., Gerhard, O. E., & Ott, T. 2000, *MNRAS*, **317**, 348
- Genzel, R., Schödel, R., Ott, T., Eckart, A., Alexander, T., Lacombe, F., Rouan, D., & Aschenbach, B. 2003, *Nature*, **425**, 934
- Gerakines, P. A., et al. 1999, *ApJ*, **522**, 357
- Ghez, A. M., et al. 2008, *ApJ*, **689**, 1044
- Gillessen, S., Eisenhauer, F., Trippe, S., Alexander, T., Genzel, R., Martins, F., & Ott, T. 2009, *ApJ*, **692**, 1075
- Gillessen, S., et al. 2006, *ApJ*, **640**, L163
- Gosling, A. J., Bandyopadhyay, R. M., & Blundell, K. M. 2009, *MNRAS*, **394**, 2247
- Groenewegen, M. A. T. 2008, *A&A*, **488**, 935
- Groenewegen, M. A. T., Udalski, A., & Bono, G. 2008, *A&A*, **481**, 441
- Guesten, R., Genzel, R., Wright, M. C. H., Jaffe, D. T., Stutzki, J., & Harris, A. I. 1987, *ApJ*, **318**, 124
- He, L., Whittet, D. C. B., Kilkenny, D., & Spencer Jones, J. H. 1995, *ApJS*, **101**, 335
- Henry, J. P., Depoy, D. L., & Becklin, E. E. 1984, *ApJ*, **285**, L27
- Hornstein, S. D., Matthews, K., Ghez, A. M., Lu, J. R., Morris, M., Becklin, E. E., Rafelski, M., & Baganoff, F. K. 2007, *ApJ*, **667**, 900
- Hummer, D. G., & Storey, P. J. 1987, *MNRAS*, **224**, 801
- Indebetouw, R., et al. 2005, *ApJ*, **619**, 931
- Jiang, B. W., Gao, J., Omont, A., Schuller, F., & Simon, G. 2006, *A&A*, **446**, 551
- Jiang, B. W., Omont, A., Ganesh, S., Simon, G., & Schuller, F. 2003, *A&A*, **400**, 903
- Kemper, F., Vriend, W. J., & Tielens, A. G. G. M. 2004, *ApJ*, **609**, 826
- Kenyon, S. J., Lada, E. A., & Barsony, M. 1998, *AJ*, **115**, 252
- Knez, C., et al. 2005, *ApJ*, **635**, L145
- Krabbe, A., Genzel, R., Drapatz, S., & Rotaciuc, V. 1991, *ApJ*, **382**, L19
- Landini, M., Natta, A., Salinari, P., Oliva, E., & Moorwood, A. F. M. 1984, *A&A*, **134**, 284
- Li, A. 2005, *ApJ*, **622**, 965
- Li, A. 2007, in *ASP Conf. Ser. 373, The Central Engine of Active Galactic Nuclei*, ed. L. C. Ho & J.-W. Wang (San Francisco, CA: ASP), **561**
- Li, A., & Draine, B. T. 2001, *ApJ*, **554**, 778
- Li, A., & Greenberg, J. M. 1997, *A&A*, **323**, 566
- Liu, T., Becklin, E. E., Henry, J. P., & Simons, D. 1993, *AJ*, **106**, 1484
- Lo, K. Y., & Claussen, M. J. 1983, *Nature*, **306**, 647
- Lombardi, M., Alves, J., & Lada, C. J. 2006, *A&A*, **454**, 781
- Lord, S. D. 1992, *NASA Technical Memorandum*
- Lutz, D. 1999, in *The Universe as Seen by ISO*, ed. P. Cox & M. Kessler (ESA Special Publication, Vol. 427; Noordwijk: ESA), **623**
- Lutz, D., et al. 1996, *A&A*, **315**, L269
- Maeda, Y., et al. 2002, *ApJ*, **570**, 671
- Maillard, J. P., Paumard, T., Stolovy, S. R., & Rigaut, F. 2004, *A&A*, **423**, 155
- Maiolino, R., Marconi, A., Salvati, M., Risaliti, G., Severgnini, P., Oliva, E., La Franca, F., & Vanzì, L. 2001, *A&A*, **365**, 28
- Marshall, D. J., Robin, A. C., Reylé, C., Schultheis, M., & Picaud, S. 2006, *A&A*, **453**, 635
- Martins, F., Genzel, R., Hillier, D. J., Eisenhauer, F., Paumard, T., Gillessen, S., Ott, T., & Trippe, S. 2007, *A&A*, **468**, 233
- Mathis, J. S. 1990, *ARA&A*, **28**, 37
- Mathis, J. S. 1996, *ApJ*, **472**, 643
- Mathis, J. S., Rimpl, W., & Nordsieck, K. H. 1977, *ApJ*, **217**, 425
- Matsunaga, N., Kawadu, T., Nishiyama, S., Nagayama, T., Hatano, H., Tamura, M., Glass, I. S., & Nagata, T. 2009, *MNRAS*, **399**, 1709
- Messineo, M., Habing, H. J., Menten, K. M., Omont, A., Sjouwerman, L. O., & Bertoldi, F. 2005, *A&A*, **435**, 575
- Mezger, P. G., Duschl, W. J., & Zylka, R. 1996, *A&AR*, **7**, 289
- Moneti, A., Cernicharo, J., & Pardo, J. R. 2001, *ApJ*, **549**, L203
- Moore, T. J. T., Lumsden, S. L., Ridge, N. A., & Puxley, P. J. 2005, *MNRAS*, **359**, 589
- Morrison, R., & McCammon, D. 1983, *ApJ*, **270**, 119
- Naoki, T., et al. 2006, *ApJ*, **640**, 373
- Naoki, T., et al. 2007, *ApJ*, **658**, 1114
- Nishiyama, S., Nagata, T., Tamura, M., Kandori, R., Hatano, H., Sato, S., & Sugitani, K. 2008, *ApJ*, **680**, 1174



- Nishiyama, S., Tamura, M., Hatano, H., Kato, D., Tanabé, T., Sugitani, K., & Nagata, T. 2009, *ApJ*, **696**, 1407
- Nishiyama, S., et al. 2006a, *ApJ*, **638**, 839
- Nishiyama, S., et al. 2006b, *ApJ*, **647**, 1093
- Paumard, T., et al. 2006, *ApJ*, **643**, 1011
- Pendleton, Y. J., & Allamandola, L. J. 2002, *ApJS*, **138**, 75
- Philipp, S., Zylka, R., Mezger, P. G., Duschl, W. J., Herbst, T., & Tuffs, R. J. 1999, *A&A*, **348**, 768
- Porquet, D., et al. 2008, *A&A*, **488**, 549
- Predehl, P., & Schmitt, J. H. M. M. 1995, *A&A*, **293**, 889
- Racca, G., Gómez, M., & Kenyon, S. J. 2002, *AJ*, **124**, 2178
- Ramírez, S. V., Arendt, R. G., Sellgren, K., Stolovy, S. R., Cotera, A., Smith, H. A., & Yusef-Zadeh, F. 2008, *ApJS*, **175**, 147
- Rawlings, M. G., Adamson, A. J., & Whittet, D. C. B. 2003, *MNRAS*, **341**, 1121
- Reid, M. J. 1993, *ARA&A*, **31**, 345
- Revnivtsev, M., van den Berg, M., Burenin, R., Grindlay, J. E., Karasev, D., & Forman, W. 2010, *A&A*, **515**, A49
- Rieke, G. H., & Lebofsky, M. J. 1985, *ApJ*, **288**, 618
- Rieke, G. H., Rieke, M. J., & Paul, A. E. 1989, *ApJ*, **336**, 752
- Rieke, M. J. 1999, in ASP Conf. Ser. 186, *The Central Parsecs of the Galaxy*, ed. H. Falcke, A. Cotera, W. J. Duschl, F. Melia, & M. J. Rieke (San Francisco, CA: ASP), 32
- Roberts, D. A., & Goss, W. M. 1993, *ApJS*, **86**, 133
- Roberts, D. A., Goss, W. M., van Gorkom, J. H., & Leahy, J. P. 1991, *ApJ*, **366**, L15
- Roberts, D. A., Yusef-Zadeh, F., & Goss, W. M. 1996, *ApJ*, **459**, 627
- Roche, P. F., & Aitken, D. K. 1984, *MNRAS*, **208**, 481
- Roche, P. F., & Aitken, D. K. 1985, *MNRAS*, **215**, 425
- Roelfsema, P. R., Goss, W. M., & Mallik, D. C. V. 1992, *ApJ*, **394**, 188
- Román-Zúñiga, C. G., Lada, C. J., Muench, A., & Alves, J. F. 2007, *ApJ*, **664**, 357
- Rosa, M. R., Zinnecker, H., Moneti, A., & Melnick, J. 1992, *A&A*, **257**, 515
- Rosenthal, D., Bertoldi, F., & Drapatz, S. 2000, *A&A*, **356**, 705
- Sakano, M., Warwick, R. S., Decourchelle, A., & Predehl, P. 2004, *MNRAS*, **350**, 129
- Salaris, M., & Girardi, L. 2002, *MNRAS*, **337**, 332
- Savage, B. D., & Mathis, J. S. 1979, *ARA&A*, **17**, 73
- Schlaflly, E. F., Finkbeiner, D. P., Schlegel, D. J., Jurić, M., Ivezić, Ž., Gibson, R. R., Knapp, G. R., & Weaver, B. A. 2010, *ApJ*, **725**, 1175
- Schödel, R., Najarro, F., Muzic, K., & Eckart, A. 2010, *A&A*, **511**, A18
- Schreiber, J., Thatte, N., Eisenhauer, F., Tecza, M., Abuter, R., & Horrobin, M. 2004, in ASP Conf. Ser. 314, *Astronomical Data Analysis Software and Systems (ADASS) XIII*, ed. F. Ochsenbein, M. G. Allen, & D. Egret (San Francisco, CA: ASP), 380
- Schultz, G. V., & Wiemer, W. 1975, *A&A*, **43**, 133
- Scoville, N. Z., Stolovy, S. R., Rieke, M., Christopher, M., & Yusef-Zadeh, F. 2003, *ApJ*, **594**, 294
- Shukla, H., Yun, M. S., & Scoville, N. Z. 2004, *ApJ*, **616**, 231
- Snedden, C., Gehrz, R. D., Hackwell, J. A., York, D. G., & Snow, T. P. 1978, *ApJ*, **223**, 168
- Stead, J. J., & Hoare, M. G. 2009, *MNRAS*, **400**, 731
- Straizys, V., & Laugalys, V. 2008, *Balt. Astron.*, **17**, 253
- Sumi, T. 2004, *MNRAS*, **349**, 193
- Sutton, E. C., Danchi, W. C., Jaminet, P. A., & Masson, C. R. 1990, *ApJ*, **348**, 503
- Tamblyn, P., Rieke, G. H., Hanson, M. M., Close, L. M., McCarthy, D. W., Jr., & Rieke, M. J. 1996, *ApJ*, **456**, 206
- Thuan, T. X., Sauvage, M., & Madden, S. 1999, *ApJ*, **516**, 783
- Tokunaga, A. T., & Vacca, W. D. 2005, *PASP*, **117**, 421
- Tran, Q. D., et al. 2001, *ApJ*, **552**, 527
- Trippe, S., et al. 2008, *A&A*, **492**, 419
- Udalski, A. 2003, *ApJ*, **590**, 284
- van Breemen, J. M., et al. 2011, *A&A*, **526**, 152
- Viehmann, T., Eckart, A., Schödel, R., Moutaka, J., Straubmeier, C., & Pott, J.-U. 2005, *A&A*, **433**, 117
- Voshchinnikov, N. V., Il'in, V. B., Henning, T., & Dubkova, D. N. 2006, *A&A*, **445**, 167
- Weingartner, J. C., & Draine, B. T. 2001, *ApJ*, **548**, 296
- Whittet, D. C. B. 1988, *MNRAS*, **230**, 473
- Whittet, D. C. B., Bode, M. F., Longmore, A. J., Adamson, A. J., McFadzean, A. D., Aitken, D. K., & Roche, P. F. 1988, *MNRAS*, **233**, 321
- Whittet, D. C. B., et al. 1997, *ApJ*, **490**, 729
- Wieprecht, E., et al. 1998, in ASP Conf. Ser. 145, *Astronomical Data Analysis Software and Systems VII*, ed. R. Albrecht, R. N. Hook, & H. A. Bushouse (San Francisco, CA: ASP), 279
- Willner, S. P., Russell, R. W., Puetter, R. C., Soifer, B. T., & Harvey, P. M. 1979, *ApJ*, **229**, L65
- Yusef-Zadeh, F., Roberts, D. A., & Biretta, J. 1998, *ApJ*, **499**, L159
- Yusef-Zadeh, F., & Wardle, M. 1993, *ApJ*, **405**, 584
- Zasowski, G., et al. 2009, *ApJ*, **707**, 510
- Zubko, V., Dwek, E., & Arendt, R. G. 2004, *ApJS*, **152**, 211